Orographic Precipitation Forcing along the Coast of Northern California during a Landfalling Winter Storm

RAUL A. VALENZUELA

Department of Atmospheric and Oceanic Sciences, and Cooperative Institute for Research in Environmental Sciences, University of Colorado, Boulder, Colorado

DAVID E. KINGSMILL

Cooperative Institute for Research in Environmental Sciences, University of Colorado, and NOAA/Earth System Research Laboratory, Boulder, Colorado

(Manuscript received 27 October 2014, in final form 27 April 2015)

ABSTRACT

This study documents orographic precipitation forcing along the coastal mountains of Northern California during the landfall of a significant winter storm over the period 16–18 February 2004. The primary observing asset is a scanning X-band Doppler radar deployed on the coast at Fort Ross, California, which provides low-level (e.g., below 1 km MSL) horizontal and vertical scans of radial velocity and reflectivity to characterize airflow and precipitation structures. Further context is provided by a wind-profiling radar, a radio acoustic sounding system (RASS), balloon soundings, buoys, a GPS receiver, and surface meteorological sensors. The winter storm is divided into two episodes, each having pre-cold-frontal low-level jet (LLJ) structures and atmospheric river characteristics. Episode 1 has a corridor of terrain-trapped airflow (TTA) that forms an interface with the LLJ. The interface extends ~25 km offshore in a ~0.5-km vertical layer, and the western edge of this interface near the ocean surface advances toward the coast over the course of ~5 h. The TTA acts as a dynamically driven barrier, so that the incoming LLJ slopes upward offshore below 1.5 km MSL and precipitation is enhanced over the ocean and near the coast. The absence of a TTA in episode 2 allows the cross-barrier flow to slope upward and enhance precipitation directly over the coastal mountains. A theoretical analysis favors the hypothesis that a gap flow exiting the Petaluma Gap forces the TTA.

1. Introduction

During the winter season, extratropical cyclones and cold fronts often develop over the northern Pacific Ocean and move toward the West Coast of the United States. A particular airflow embedded within these cyclones, known as the warm conveyor belt, is associated with significant precipitation events along the West Coast mountain ranges. Warm conveyor belts extend over a broad area ahead of surface cold fronts and are associated with poleward heat transport (latent and sensible heat) and isentropic ascent over the surface warm front (Harrold 1973; Schultz 2001; Eckhardt et al. 2004). In addition, they usually present a horizontal wind speed profile with a local maximum at an average altitude of ~1 km MSL, referred to as the low-level jet (LLJ, e.g., Neiman et al. 2002; Ralph et al. 2005). More recently, a narrow subset of the warm conveyor belt coincident with the LLJ core and associated with large horizontal water vapor transport has been documented. This structure is now commonly referred to as an atmospheric river (AR; Zhu and Newell 1994; Ralph et al. 2004, 2005). Winter-season ARs offshore of the U.S. West Coast are on average oriented with their long axis from southwest to northeast (Neiman et al. 2008, Wick et al. 2013).

Many West Coast mountain ranges can be approximated as nearly two-dimensional barriers. Those in Northern California, such as the Sierra Nevada and nearby coastal ranges, have a generally northwest-to-southeast orientation. Such a topographic characteristic allows the typical AR to impact the mountains with a near-perpendicular orientation, favoring the cross-barrier ascent of moist, statically neutral air (Neiman

Corresponding author address: Raul A. Valenzuela, University of Colorado, ATOC, UCB 311, Boulder, CO 80309.
E-mail: raul.valenzuela@colorado.edu

DOI: 10.1175/MWR-D-14-00365.1

et al. 2002; Ralph et al. 2005). However, this relatively simple orographic precipitation forcing can become more complicated when a low-level terrain-trapped airflow exists. A terrain-trapped airflow (TTA) is defined as a relatively narrow air mass consistently flowing in close proximity and approximately parallel to an orographic barrier. Within the context of Pacific winter storms making landfall along the West Coast, TTAs flow poleward along the western side of coastal mountain ranges.

One mechanism often attributed to TTA formation is low-level blocking (Smith 1979). In this scenario, stably stratified air parcels decelerating and abutting the windward slope of a mountain are unable to surmount the barrier and instead turn left (right) in the Northern (Southern) Hemisphere as a result of an increasing along-barrier pressure gradient and weakened Coriolis force. Theoretical studies (e.g., Pierrehumbert and Wyman 1985) have shown that an airflow impinging on a two-dimensional barrier can be described by the nondimensional Froude number (Fr):

$$\mathrm{Fr} = \frac{U}{Nh}, \tag{1}$$

where N represents the Brunt–Väisälä frequency within the stable air, h the barrier height, and U the cross-barrier wind speed upstream of the stable air and orthogonal to the terrain. The Fr values between 0 and 1 indicate favorable conditions for the formation of low-level blocking.

TTAs can also be induced by gap flows. Gap flows are usually produced in mountainous regions when a relatively cold continental air mass crosses through gaps (i.e., narrow topographic depressions) as a response to an along-gap pressure gradient associated with approaching synoptic-scale disturbances (e.g., Lackmann and Overland 1989; Neiman et al. 2006; Mayr et al. 2007). Mass et al. (1995, henceforth M95) derived an analytical expression for gap flows that includes both pressure-gradient forces and frictional effects:

$$u^2(x) = \left[u^2(0) - \frac{\mathrm{PGF}}{K}\right] e^{-2Kx} + \frac{\mathrm{PGF}}{K}. \tag{2}$$

Here, $u(0)$ and $u(x)$ represent the airflow at the entrance and at some distance x downstream from the gap entrance (respectively), PGF is the along-gap pressure gradient force ($-\rho^{-1}\partial P/\partial x$), and $K = 2.8C_D/H$ is a parameter representing friction through a drag coefficient (C_D) and the average depth of the boundary layer within the gap (H). After exiting the mountain barrier, gap flows are able to turn to the right (left) in the Northern (Southern) Hemisphere with a radius of curvature determined by their wind speed and the Coriolis parameter (e.g., Steenburgh et al. 1998). This effect can be enhanced when an offshore-directed gap flow joins a large-scale onshore-directed airflow, a phenomenon observed by Loescher et al. (2006) along the coast of Alaska.

A detailed understanding of TTA kinematic structure is essential for clarifying how TTAs impact the intensity and spatial distribution of orographic precipitation, which ultimately can help improve forecasts of storms that have the potential to cause flooding and debris flows in midlatitude mountainous regions (Ralph et al. 2006; Neiman et al. 2009). For example, Bousquet and Smull (2003) attributed the errors in a severe precipitation forecast in the Alps to an inadequate representation of a blocking-induced TTA in the model. Likewise, Neiman et al. (2002, 2004), Yu and Bond (2002), Anders et al. (2007), and Hughes et al. (2009) have documented the effects of blocking-induced TTAs on the spatial distribution of precipitation.

TTAs produced by gap flows have also been studied (e.g., Overland and Walter 1981; Overland 1984; Lackmann and Overland 1989; Mass et al. 1995; Steenburgh et al. 1998; Colle and Mass 2000) but few of these investigations have focused on the association of gap flows with orographic precipitation. In one of these rare studies, Neiman et al. (2006) examined 915-MHz wind profiler observations along the coast of Northern California at Bodega Bay during winter storms from 1997 to 2004. They found that a cold and dry airstream of ~500-m depth frequently exited through the Petaluma Gap and that total rainfall and rain rates increased over Bodega Bay during strong gap-flow cases.

Compared to inland ranges such as the Cascades and Sierra Nevada, coastal ranges in the western United States are impacted by landfalling ARs unperturbed by upstream terrain. This relative simplicity has motivated the observational documentation of orographic precipitation mechanisms during winter storms along coastal ranges. For example, Yu and Smull (2000) examined a case where the pre-cold-frontal air was associated with a weak TTA within ~20 km offshore of the Oregon–California coastal mountains and enhanced precipitation along the coast. Also, Neiman et al. (2002) found a statistically significant linear relationship between cross-barrier wind speed in the LLJ at ~1 km MSL and rain rate at the surface using two winter seasons of observations along the windward side of Northern, central, and Southern California coastal ranges. Remarkably, the linear relationship below mountaintop was degraded at lower levels when hypothesized blocking-induced TTAs were evident. James and Houze (2005) documented coastal orographic precipitation enhancement during three winter seasons along the Oregon–California border, hypothesizing that offshore enhancement was associated with TTAs.

The aforementioned studies provide clues about the structure of TTAs adjacent to coastal orography and the associated impacts on precipitation but were limited in a few important respects. For example, the results of Neiman et al. (2002, 2006) were based on a one-dimensional, vertical-profile perspective. Also, the studies of Yu and Smull (2000) and James and Houze (2005), although based on scanning radars, had incomplete documentation of airflows below the peaks of the coastal orography, which prevents the detailed examination of low-level three-dimensional kinematic structures that are essential for better understanding their influence on orographic precipitation. The present investigation addresses these limitations by observationally documenting a landfalling winter storm along the Northern California coast with a combination of scanning and profiling radar data obtained with ground-based instrumentation deployed near sea level. This study is unique because it documents in detail the three-dimensional kinematic structure and orographic precipitation forcing at low levels (e.g., below 1 km MSL) associated with a small-scale coastal barrier. Section 2 provides information about the observing systems and data processing employed in this study. An overview of the storm is presented in section 3, with synoptic context for the mesoscale observations. Section 4 contains a detailed analysis of the kinematic and precipitation structure of the storm, which is separated into two distinct episodes. The theoretical context for the observed airflow structures is discussed in section 5. Finally, section 6 presents a summary and conclusions for this study.

2. Observing systems and data processing

The data employed in this study were collected along the Northern California coast during the 2003/04 winter season as part of the Hydrometeorology Testbed (HMT; Ralph et al. 2013) operated by the National Oceanic and Atmospheric Administration (NOAA). Locations of key observing systems are shown in Fig. 1a. The primary instrument used in this study is the scanning ground-based NOAA X-band (3.2-cm wavelength) dual-polarization Doppler radar called X-Pol (Martner et al. 2001; Matrosov et al. 2005) deployed at Fort Ross, California (FRS).

The X-Pol radar executed both slant-horizontal plan-position indicator (PPI) and vertically oriented range–height indicator (RHI) scans (Table 1). PPI scans extended to a maximum range of 57 km with 0.23-km gate spacing and were repeated at least once every 6 min. At elevation angles ≤9.0°, PPI scans were only directed offshore as a result of low-level beam obstruction by the coastal mountains. RHI scans extended to a maximum range of 29 km with 0.11-km gate spacing and were executed over the ocean and terrain in a cycle that repeated at least once every 6 min.

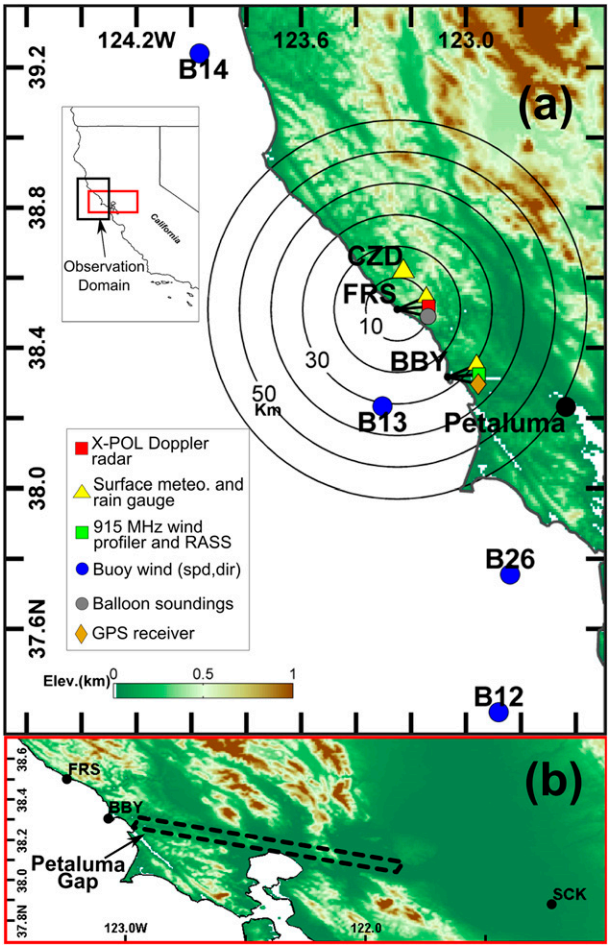

FIG. 1. (a) Topographic map overlaid with observing systems. Legend identifying each instrument along with the color scale for terrain elevation (km) is located at the bottom-left corner. Range circles centered at FRS indicate the X-Pol analysis domain. (b) Topographic map showing Petaluma Gap terrain and the METAR station at SCK. Inset map in (a) provides a reference for both topographic maps relative to the coast of Northern California: map (a), black line; map (b), red line.

Individual sweeps were edited to remove artifacts such as ground and sea clutter, range folding (i.e., second trip echoes), and sidelobe echoes, as well as to dealias folded radial velocities. After editing, polar-coordinate scans were interpolated onto a Cartesian grid. For PPI scans, the horizontal and vertical grid spacings were 0.5 and 0.35 km, respectively. For RHI scans, the horizontal grid spacing was 0.1 km and the vertical grid spacing was 0.2 km. A Cressman distance-dependent weighting scheme (Trapp and Doswell 2000) was employed to interpolate values of attenuation-corrected reflectivity

TABLE 1. PPI and RHI scan strategies performed by X-Pol.

	Rotation angle	Fixed angle
	Azimuth (°)	Elev (°)
PPI	150–330	0.5, 1.0, 2.0, 3.4, 4.8, 6.2, 7.6, 9.0
	0–360	11.0, 13.0, 15.0, 17.0, 19.0
	Elev (°)	Azimuth (°)
RHI	0–100	0, 15, 30, 45, 60, 75, 90, 105, 120, 135, 150, 180, 210, 240, 270, 300, 330, 345
	0–162	6, 147

(Matrosov et al. 2005) and Doppler radial velocity to each Cartesian grid point.

Composite vertical cross sections of reflectivity and radial velocity were made by combining north and south RHI scans (e.g., 0° and 180° azimuth). Although the contributing RHI scans were offset by 2–3 min, the structure across the interface of the two scans was coherent. The horizontal component of radial velocity in the plane of each composite cross section was calculated toward north (i.e., meridional wind). Elevation angles greater than 30° were excluded to simplify both visualization and interpretation of airflow structures.

A velocity–azimuth display technique (VAD; Browning and Wexler 1968) was applied to 15°-elevation-angle PPI scans, with one scan available every 12 min. The VAD technique allows the retrieval of mean horizontal wind above and centered on the radar by using Fourier analysis of the radial velocity as a function of azimuth. Radial velocities from slant ranges between 0.3 and 8 km were employed to derive VAD wind profiles from near the surface up to ~2 km MSL.

A 915-MHz wind-profiling radar (Ecklund et al. 1988; Carter et al. 1995) located at Bodega Bay (BBY; Fig. 1a) provided hourly profiles of horizontal winds from ~0.1 to ~2.3 km MSL with ~60-m vertical resolution (low-altitude mode). Hourly wind profiler data were processed with the continuity method of Weber et al. (1993) that checks consistency in the dataset over time and height. To complement the wind profiler at BBY, a radio acoustic sounding system (RASS) was also deployed at this site, retrieving hourly profiles of virtual temperature (Clifford et al. 1994). The system retrieved a total of 20 range gates from 141 to 1268 m MSL at ~60-m intervals. Hourly RASS data were processed using the consensus method of Fischler and Bolles (1981) that checks for consistency in time. Virtual potential temperature was then derived using the method of Neiman et al. (1992).

Several other important observing systems contributed to the analysis. Vertical profiles of pressure, temperature, relative humidity, and horizontal wind velocity were retrieved from seven balloon soundings released at FRS with an average vertical resolution of 9 m. Routine buoy data from NOAA's National Data Buoy Center provided surface winds offshore. Buoy 46013 (henceforth B13) is located ~22 km southwest of BBY and reports hourly averaged wind speed and direction observed continuously at 1-min resolution. In addition, buoys 46014 (B14), 46026 (B26), and 46012 (B12), located ~126 km north, ~67 km south, and ~104 km south from B13, respectively, were included in the analysis (Fig. 1a). Hourly averaged column-integrated water vapor (IWV) at BBY was obtained from a ground-based global positioning system (GPS) receiver (Wolfe and Gutman 2000), allowing the evolution of water vapor to be monitored while the storm passed over the observing domain. GPS-IWV observations are unaffected by precipitation (Businger et al. 1996). Two-minute-resolution surface observations of air temperature, relative humidity, pressure, wind velocity, and precipitation were collected at FRS, BBY, and Cazadero, California (CZD). These observations were manually checked for outliers and time consistency.

3. Event overview

Analyses from the Climate Forecast System Reanalysis (CFSR; Saha et al. 2010) provide synoptic-scale context for the storm (Fig. 2). An upper-level cyclonic circulation is evident over the Pacific (~45°N, ~145°W) at 0600 UTC 16 February (Fig. 2a) and is associated with developing cold and warm fronts on its southeast flank. The warm front approaches the coast of Northern California by 1800 UTC 16 February (Fig. 2b), making landfall at 0000 UTC 17 February and then dissipating (not shown). By 0600 UTC 17 February (Fig. 2c), the cold front has stalled offshore of Northern California as a stationary front. A 500-hPa short-wave trough approaching from the west and a ridge building onshore are also evident at this time. By 1800 UTC 17 February (Fig. 2d), the short-wave trough aloft begins accelerating toward the California coast. After 1800 UTC 17 February, the short-wave trough aloft progresses quickly eastward to California and the cold front consequently moves rapidly southeastward down the California coast (Figs. 2e,f).

The characteristics of the stationary front are examined in more detail with hourly averaged winds from buoy observations (Fig. 3). There are relatively weak cold-sector winds at B14 during the period from about 2200 UTC 16 February to about 0600 UTC 17 February, with stronger warm-sector south-southeasterly winds before and after. This suggests that the stationary front sagged southward over B14 during this period and then retreated northward. B13 exhibits a similar trend, but

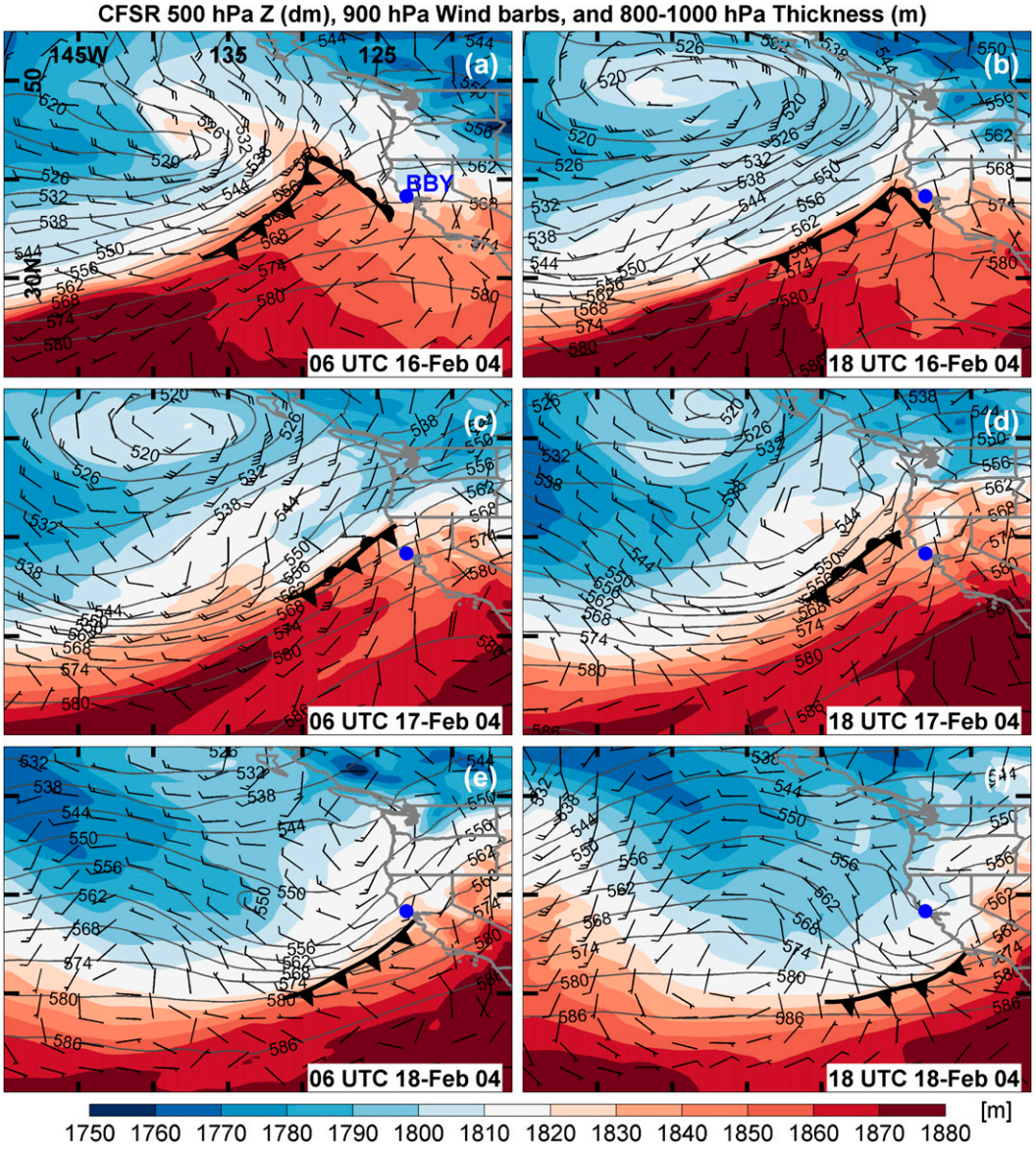

FIG. 2. Reanalysis-derived 500-hPa geopotential height (Z, contours), 900-hPa wind barbs, and 800–1000-hPa thickness (m, filled contours) from the NCEP CFSR at (left) 0600 and (right) 1800 UTC on (a),(b) 16; (c),(d) 17; and (e),(f) 18 Feb. Conventional symbols for near-surface cold, warm, and stationary fronts are included. Full barbs are 10 m s^{-1}. Blue dot indicates BBY location.

delayed by about 4 h with less of a contrast in wind characteristics and of shorter duration. Farther south, B26 and B12 show none of the effects of the stationary front given that it remained north of these buoys. After 1000 UTC 18 February, all the buoys mark a wind-velocity shift from southerly to northwesterly with the southeastward-directed cold-frontal passage (as revealed by the CFSR analyses in Fig. 2).

Additional synoptic context is provided by IWV retrievals (Wentz 1997) from the group of three polar-orbiting satellites carrying the Special Sensor Microwave Imager (SSM/I). Figure 4 presents composite images of SSM/I IWV during periods similar to those shown in Fig. 2. A long and narrow corridor of IWV greater than 2 cm is evident offshore of California during the entire storm, which is the signature of a landfalling AR (Zhu and Newell 1998; Ralph et al. 2004). Initial AR landfall occurs shortly after 0600 UTC 16 February (Fig. 4a). Thereafter, from 1400 UTC 16 February to 0800 UTC 17 February (Figs. 4b,c), the AR meanders, probably in association with the stationary front depicted by the CFSR analysis. Finally, from 1400 UTC

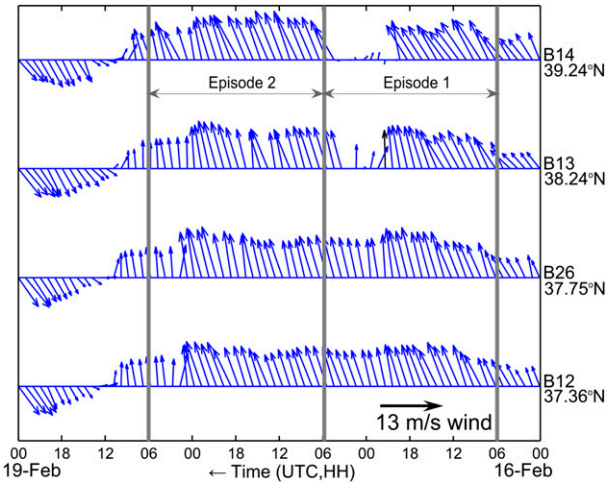

FIG. 3. Wind vectors from buoys B14 (39.24°N, 123.97°W), B13 (38.24°N, 123.30°W), B26 (37.75°N, 122.84°W), and B12 (37.36°N, 122.88°W) located offshore of the Northern California coast and arranged from north to south. Time is from right to left to represent the eastward advection of the storm. Black vector wind scale is included. See text for definition of episodes 1 and 2.

17 February onward (Figs. 4d,e,f), the AR shows a southward progression in connection with the cold frontal passage indicated by the CFSR at similar times.

Time series of surface rain-rate observations (Fig. 5a) highlight relevant meteorological characteristics in Northern California during the landfalling storm, which produced total rainfall accumulations of 252, 152, and 125 mm at CZD, FRS, and BBY, respectively. There are two distinct episodes of relatively large surface rain rate: from 0600 UTC 16 February to 0600 UTC 17 February (episode 1) and from 0600 UTC 17 February to 0600 UTC 18 February (episode 2). Peak rain rates of 3–8 mm h^{-1} are evident at all sites during episode 1 from 0600 UTC 16 February to 1500 UTC 16 February, with slightly higher values at BBY (coast) and slightly lower values at CZD (coastal mountains). Shortly thereafter, rain rates increase dramatically. Peak values of 10–20 mm h^{-1} are evident between 1500 and 2100 UTC 16 February, with the largest rain rates at CZD and the smallest at BBY. After the peak, rain rates decrease to less than 5 mm h^{-1} through the end of episode 1. In contrast to episode 1 with its single peak of rain rate, episode 2 is characterized by multiple lower-valued peaks of rain rate. Maximum rain rate at CZD is ~18 mm h^{-1} while at BBY and FRS maximum values are a factor of 3 smaller (~6 mm h^{-1}). To further contrast both episodes, Table 2 reveals that during episode 1 similar amounts of precipitation fell along the coast and over the mountains (e.g., only 10%–27% of orographic enhancement); however, episode 2 exhibits a significant difference between precipitation along the coast and the coastal mountains (e.g., 241%–393% of orographic enhancement).

Neiman et al. (2009) document that the largest correlation between cross-barrier bulk IWV flux and rain rate over the coastal mountains of Northern California is achieved in a ~300-m-deep layer centered at ~1 km MSL. Thus, the cross-barrier bulk IWV flux at BBY was computed as the product between GPS IWV and layer-mean (0.85–1.15 km MSL) cross-barrier wind speed (directed toward 50°) observed with the wind profiler (Fig. 5b). Although GPS IWV is an integrated observation of air moisture, balloon soundings (not shown) confirm that most of the water vapor (e.g., mixing ratio >6 g kg^{-1}) is on average located below 2.5 km MSL, with maximum values of ~8.5 g kg^{-1} near the surface. Figure 5b illustrates that episode 1 is associated with maximum bulk IWV flux of 80–90 cm m s^{-1} over a ~5-h period coinciding with peak rain rates, whereas episode 2 is characterized by values around 70 cm m s^{-1} over most of the period with less clear association to the rain-rate time series compared with episode 1. The peak in bulk IWV flux at the interface between episodes 1 and 2 (e.g., 0600 UTC 17 February) occurs along with rain rates near zero and is associated with relatively large cross-barrier wind speeds (~35 m s^{-1}) and a local minimum in GPS IWV (~2.7 cm). It is worth noting that, despite this single peak, the overall trend in rain rate seems better correlated with bulk IWV flux compared with GPS IWV alone, in agreement with the results of Neiman et al. (2009).

4. Detailed kinematic and precipitation structure

a. Episode 1: 0600 UTC 16 February–0600 UTC 17 February 2004

Previous studies by Ralph et al. (2004, 2005) and Neiman et al. (2002, 2009) have consistently observed the prefrontal LLJ at a height of ~1 km MSL. As indicated by CFSR analyses (Fig. 2), winds at 900 hPa (~1 km MSL) near BBY and FRS are characterized by a strong meridional component. Thus, we can infer that the LLJ in this case has a primarily meridional orientation.

Wind profiler data at BBY indicate an LLJ centered at ~1 km MSL from ~1000 to 1400 UTC 16 February (Fig. 6a). The LLJ manifests itself as a meridional-component wind speed maximum of ~25 m s^{-1} from ~0.5 to 1.5 km MSL. During the same period, a VAD analysis at FRS shows an LLJ of comparable magnitude, thickness, and altitude (Fig. 6b). After 1400 UTC 16 February, the LLJ-center descends at both locations, down to ~0.5 km MSL at BBY and down to ~0.7 km MSL at FRS. Then, both profiles show a decrease in

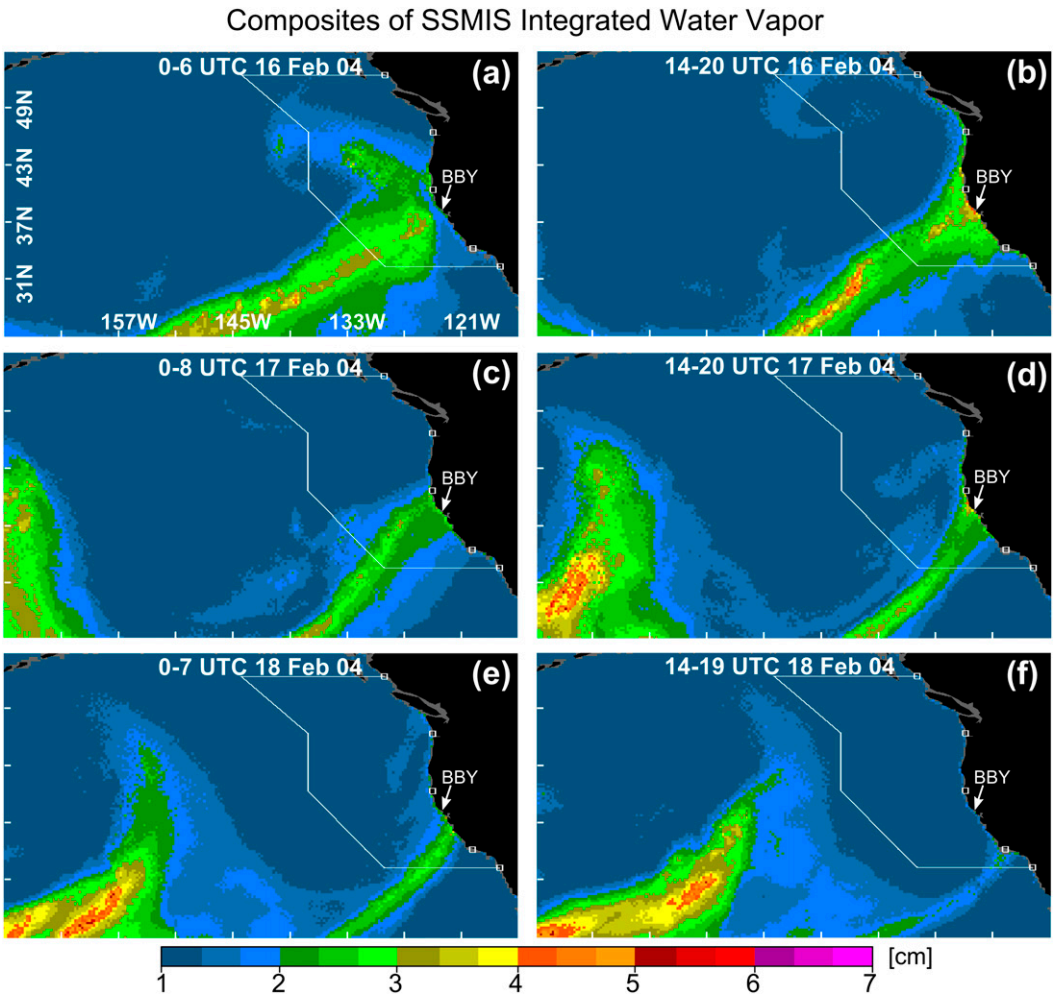

FIG. 4. IWV composite images observed with the SSM/I instrument over the periods (a) 0000–0600 UTC 16 Feb, (b) 1400–2000 UTC 16 Feb, (c) 0000–0800 UTC 17 Feb, (d) 1400–2000 UTC 17 Feb, (e) 0000–0700 UTC 18 Feb, and (f) 1400–1900 UTC 18 Feb. Color scale for IWV indicated at bottom of panels.

meridional wind speed after 2100 UTC 16 February in association with the cold frontal passage described in section 3. FRS shows the largest decrease in wind speed after 2100 UTC 16 February and both profiles return to wind speeds $>20\,m\,s^{-1}$ after 0200 UTC 17 February, which is consistent with a cold front sagging southward and retreating northward afterward (e.g., Fig. 3).

Along with the LLJ structure and cold frontal effects, both time–height cross sections show a distinctive vertical gradient of meridional wind speed centered at ~0.6–0.7 km MSL, with values of $\sim 5\,m\,s^{-1}$ below and $\sim 25\,m\,s^{-1}$ above. At BBY the gradient is observed from 0900 to 1500 UTC 16 February while at FRS the gradient is apparent at the same altitude from ~0900 to 1800 UTC 16 February. Winds below the gradient are mainly southeasterly at both sites and a jet structure is absent. This suggests that the airflow is directed approximately parallel to the terrain orientation during the periods described above and is therefore consistent with a TTA.

The horizontal pattern of Doppler radial velocity associated with the TTA during episode 1 is analyzed with hourly averaged X-Pol 0.5° PPI scans. Figure 7a depicts a representative hour (e.g., at 1400–1500 UTC 16 February) when a sharp curvature in the isoline of zero radial velocity (henceforth called the zero isodop) is evident along the ~225° radial at a range of ~18 km. This curvature indicates a nearly homogenous southeasterly wind from the coast to ~18 km offshore and a significant wind direction shift farther offshore, where the zero isodop changes its orientation by about 90°, implying south-southeasterly to southerly winds. At ~18-km range, the X-Pol 0.5° beam is at an altitude of ~220 m MSL, which is well below the vertical

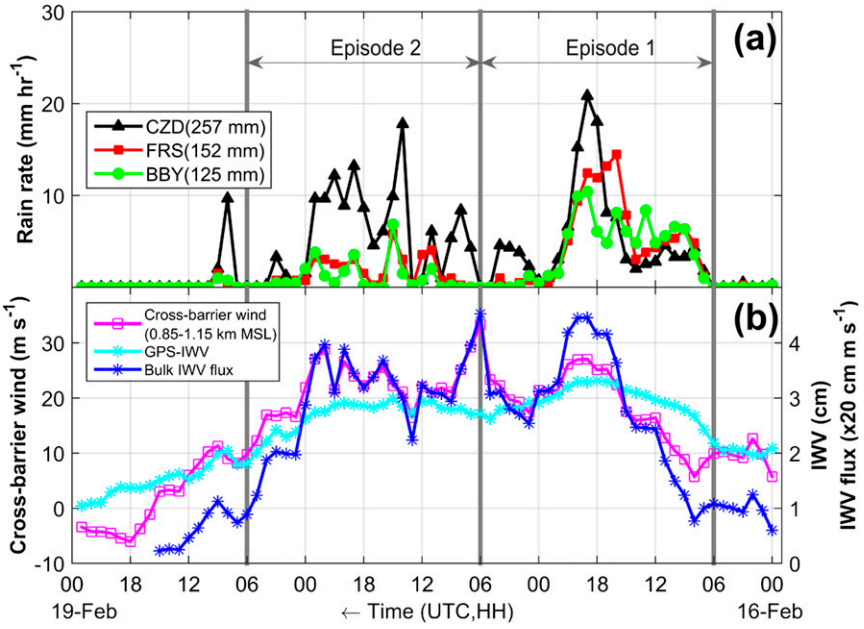

FIG. 5. (a) Rain rates at CZD (black), FRS (red), and BBY (green). Legend includes total accumulated precipitation at each site over the period from the beginning of episode 1 to the end of episode 2. (b) The 0.85–1.15 km MSL layer-mean cross-barrier wind speed (i.e., directed toward 50°) from the wind profiler along the left axis and GPS IWV and bulk IWV flux along the right axis. Bulk IWV flux is derived from the product of the layer-mean cross-barrier wind speed and the GPS IWV. Time is from right to left to represent the eastward advection of the storm. See Fig. 1 for locations of CZD, FRS, and BBY.

gradient of wind direction observed in the vertical profiles at BBY and FRS (Fig. 6). This suggests that the sharp curvature observed in the zero isodop ~18 km offshore is the result of a horizontal gradient in wind direction. Additionally, Wood and Brown (1986) simulated a variety of Doppler patterns using different wind direction and speed profiles. The only case that produced a sharp curvature in the zero-isodop line was the simulation of a horizontal wind direction discontinuity within the radar domain intended to mimic a frontal boundary. Consequently, the sharp curvature in the zero isodop is most likely due to a strong horizontal gradient in wind direction. We assert that this horizontal gradient is associated with the interface between the TTA along the coast and the LLJ farther offshore.

The companion average reflectivity (Fig. 7b) shows a precipitation pattern dominated by a band of northwest–southeast-oriented enhanced reflectivity from the coast to ~20 km offshore. This was a nearly stationary structure that persisted at other hours during episode 1 with both variable extension offshore and reflectivity magnitude. Figure 7b also shows five thinner reflectivity bands with similar orientation 20–60 km southwest of the radar and two southwest–northeast-oriented reflectivity bands on the western edge of the domain. Individual 6-min 0.5° PPI scans between 1400 and 1500 UTC 16 February (e.g., Figs. 7c,d) indicate that the former corresponds to a single northwest–southeast-oriented band moving northeastward during the averaging period, whereas the latter is formed by two isolated cells moving toward the northeast and giving the appearance of a southwest–northeast-oriented band.

Vertical context for the converging LLJ and TTA is provided by examination of X-Pol RHI scans oriented

TABLE 2. Site elevation and total precipitation during episode 1 (0600 UTC 16 Feb–0600 UTC 17 Feb) and episode 2 (0600 UTC 17 Feb–0600 UTC 18 Feb). The CZD ratio is defined as the total precipitation at CZD divided by the total precipitation at each of the three sites.

Station	Elev (m MSL)	Episode 1 (mm)	CZD ratio	Episode 2 (mm)	CZD ratio
CZD	462	124	1.00	133	1.00
FRS	40	113	1.10	39	3.41
BBY	15	98	1.27	27	4.93

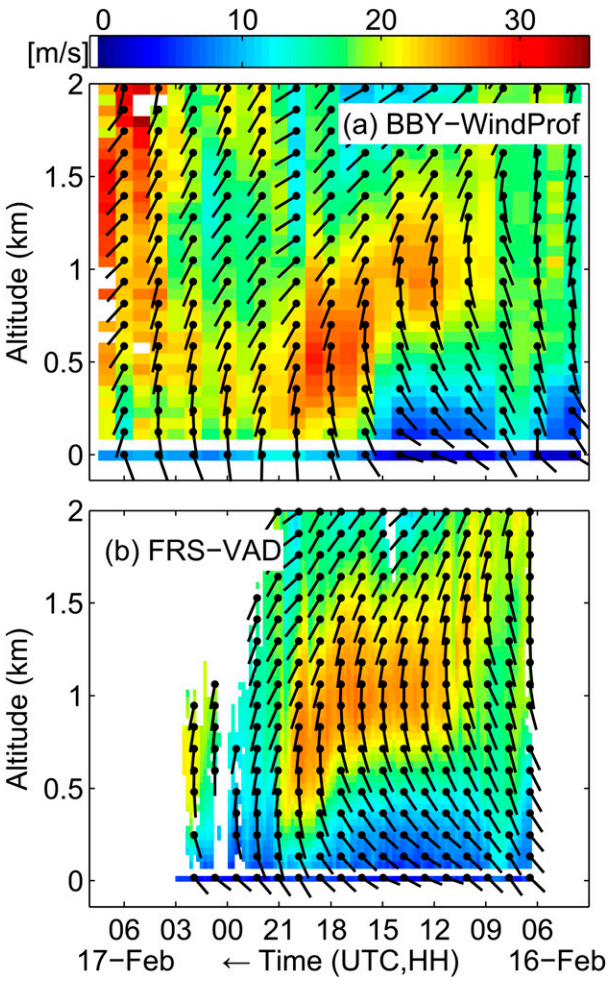

FIG. 6. Time–height analysis of meridional wind speed (color coded, $m\,s^{-1}$) and total wind direction (wind staffs) at (a) BBY from the 915-MHz wind profiler (WindProf) and (b) FRS from an X-Pol VAD analysis during episode 1. The first level in each panel includes surface observations. Time is from right to left to represent the eastward advection of the storm.

from south to north (e.g., 180°–360°). The horizontal velocity during 1400–1500 UTC 16 February (Fig. 8a) indicates a strong airflow of ~20–25 $m\,s^{-1}$ (meridional component of the LLJ) sloping over a weaker flow of ~5–10 $m\,s^{-1}$ (meridional component of the TTA). Horizontal velocity during 1700–1800 UTC 16 February (Fig. 8b) shows a similar structure but with the LLJ sloping over the weaker flow closer to the coast. Assuming that the LLJ–TTA interface near sea level is located 20–25 km offshore from the coast during 1400–1500 UTC, then the difference between the two hours shows a progression of ~15 km toward the coastline. As a result, the vertical kinematic structure at these times illustrates how the LLJ slopes upward over the TTA offshore and also how the interface between these two flows gets closer to the coast.

The average vertical structure of reflectivity gives some clues about the precipitation structure associated with the LLJ–TTA interface. During 1400–1500 UTC 16 February (Fig. 8c), there is evidence of a bright band (i.e., melting layer) at ~3 km MSL that ascends slightly toward the coastal mountains. This upward deviation of the bright band toward the mountains is opposite of that typically observed in association with larger barriers (e.g., Marwitz 1983; Minder and Kingsmill 2013). The physical mechanisms responsible for this behavior are unclear. Above and below the bright band some vertically oriented reflectivity structures resembling fallstreaks are observed. The presence of a bright band and fallstreaks suggests that seeder particles aloft are available to fall into feeder clouds at lower levels and contribute to precipitation development via the seeder–feeder process (e.g., Bergeron 1965; Browning et al. 1974; Rutledge and Hobbs 1983). Below ~1.5 km MSL and from ~2.5 to ~18 km offshore there is a concentrated area of enhanced precipitation. Interestingly, the enhancement below ~1.5 km MSL resides downwind from where the LLJ slopes upward (Fig. 8a). This suggests that precipitation enhancement is associated with condensate production resulting from lifting of the LLJ by the TTA. Later, during 1700–1800 UTC 16 February (Fig. 8d), the precipitation enhancement zone is closer to the coast and more intense, especially over the windward side of the coastal mountains. Accordingly, an upslope flow effect (i.e., direct orographic ascent) likely has a larger role going forward from this time.

Isochrones of the zero isodop are drawn every 2 h from 0800 to 2100 UTC 16 February to analyze the motion of the LLJ–TTA interface over the course of episode 1 (Fig. 9). The zero isodop changed its shape significantly during this period. It started as a nearly straight, west-southwest to east-northeast line between 0800 and 0900 UTC 16 February. Thereafter, zero-isodop lines attained an increasingly curved appearance with their western extent moving progressively northward and closer to the coast. A short segment of sharp curvature in the zero-isodop lines was first observed during 1400–1500 UTC 16 February at ~18-km range. It is this sharp curvature that is most indicative of the wind discontinuity associated with the LLJ–TTA interface. Later isochrones also exhibit short segments of sharp curvature, but they occur closer to the coastline. This implies that the LLJ–TTA interface moves toward the shore over time. By 2000–2100 UTC 16 February, the zero-isodop line is so close to the coastline and its length so truncated that the LLJ–TTA interface is difficult to see in the X-Pol PPI data.

If the TTA is causing a horizontal wind discontinuity detectable in the Doppler velocity pattern, then variations

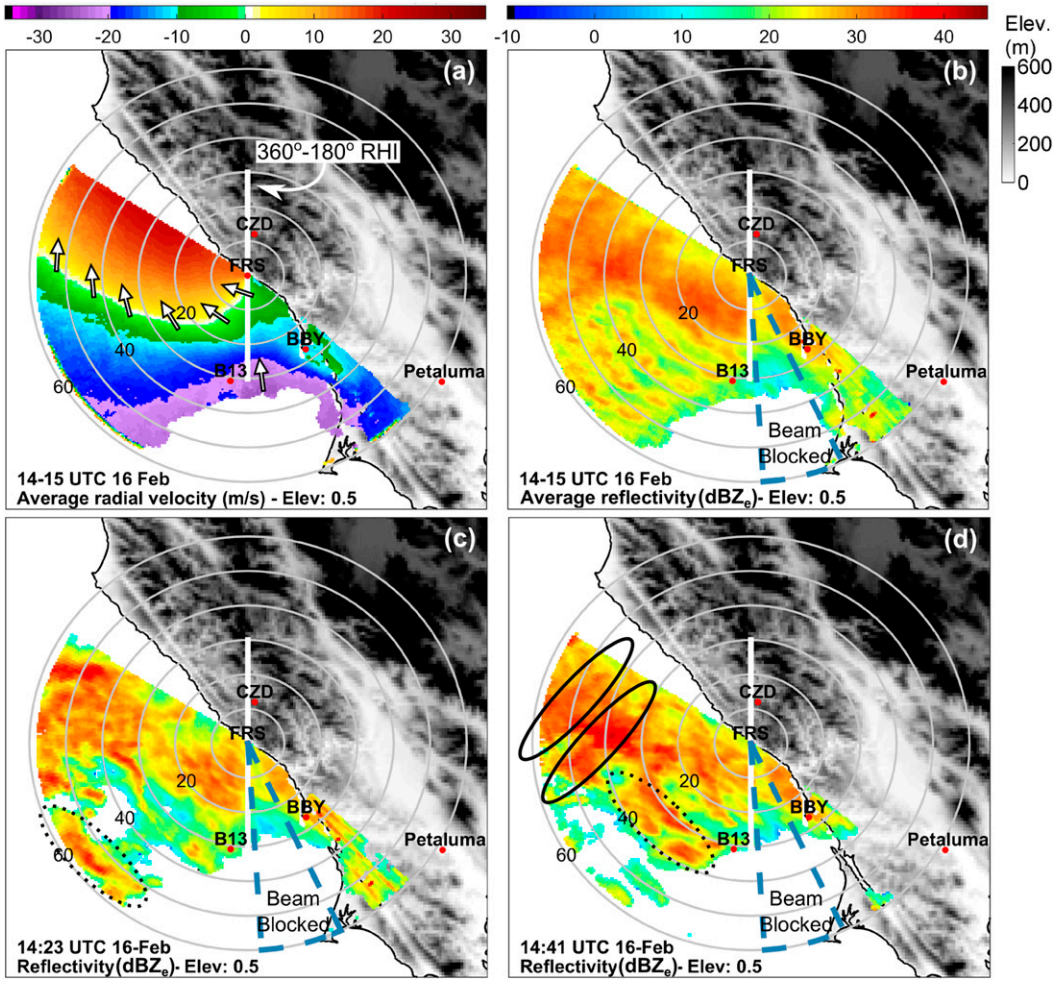

FIG. 7. (a) Average radial velocity ($m\,s^{-1}$) and (b) equivalent reflectivity (dBZ_e) from PPI scans observed during episode 1 between 1400 and 1500 UTC 16 Feb. Individual scans of equivalent reflectivity at (c) 1423 and (d) 1441 UTC 16 Feb. Arrows along the isoline of zero radial velocity (zero isodop) in (a) are orthogonal to X-Pol beams; thus they aid in visualizing the airflow direction. The isolated arrow along the ~170° radial at ~30-km range in (a) indicates the direction of maximum approaching radial velocities (~25 $m\,s^{-1}$) associated with the LLJ. The dashed line sector in (b)–(d) indicates an area with decreased reflectivity due to beam blockage by the radar trailer. Transient reflectivity bands oriented northwest–southeast (dotted line) and southwest–northeast (continuous line) are highlighted in (c) and (d), which are visualized in the 1400–1500 UTC average (b). Panels include the azimuth direction (white line) of RHI analyses for episode 1 (see Fig. 8).

in the Doppler pattern from one time to another might provide information about the wind-discontinuity motion. Variations in the Doppler pattern were quantified by computing hourly standard deviations of radial velocity from single PPI scans with 0.5°-elevation angle. The hourly standard deviation of Doppler radial velocity (StdDev) between 1400 and 1500 UTC 16 February (Fig. 10a) is in general at or below ~1 $m\,s^{-1}$ except for a northwest–southeast-oriented band of large variability with values around 2 $m\,s^{-1}$ or greater. Along with the information provided by the hourly averaged radial velocity, this standard-deviation band (henceforth called the StdDev band) identifies the location and progression of the LLJ–TTA interface between 1400 and 1500 UTC 16 February. In other words, the interface was northwest–southeast-oriented and moved a distance equivalent to the StdDev bandwidth (i.e., from the ~25- to ~18-km range ring) toward the northeast. Figure 10b shows isochrones of the LLJ–TTA interface from 1300 to 1800 UTC 16 February, indicating that the interface propagated ~22 km toward the coast over 5 h, which represents an average speed of ~1.2 $m\,s^{-1}$. This means that the interface approaches the coast at a slower speed than the background south-southeasterly

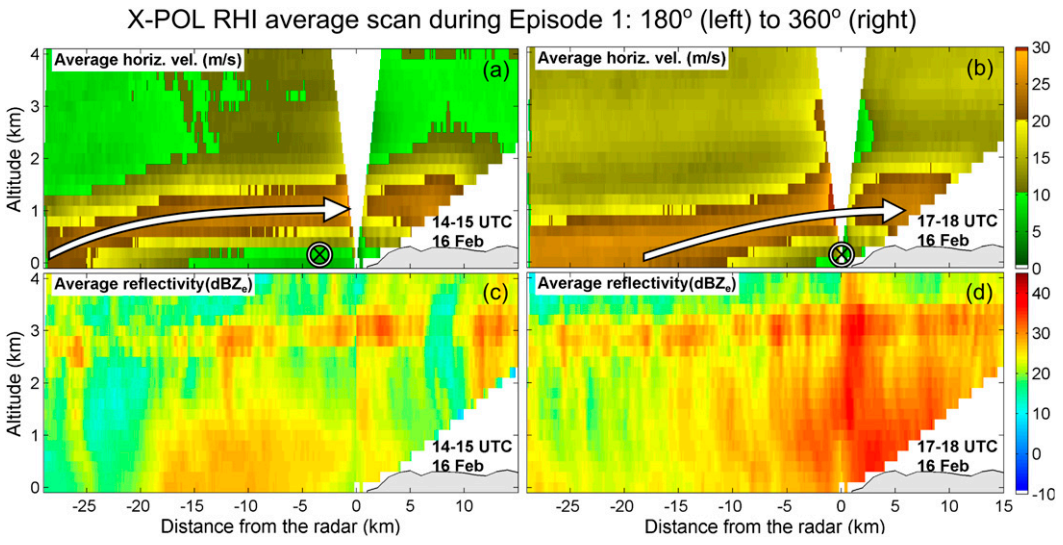

FIG. 8. (a),(b) Average horizontal velocity ($m\,s^{-1}$; see color scale) and (c),(d) equivalent reflectivity (dBZ_e; see color scale) from RHI scans observed during episode 1 between (left) 1400 and 1500 UTC and (right) 1700 and 1800 UTC 16 Feb in the meridional direction (180°–360° azimuth, indicated in Fig. 7). White arrows in horizontal velocity indicate the location of the LLJ, whereas the crossed circle indicates the location of the TTA.

airflow of ~12–15 $m\,s^{-1}$ at the surface (indicated by B13) and the south-southeasterly airflow of ~20–25 $m\,s^{-1}$ at ~250 m MSL (indicated by the PPI and RHI scans). In addition, the isochrones point out that the LLJ–TTA interface has a skewed orientation relative to the mean coastline orientation during the course of episode 1, with positions that are farther offshore toward the north.

The precipitation response to the LLJ–TTA interface motion is investigated by using a contoured frequency by distance diagram (CFDD) of reflectivity for each hour during episode 1. Unlike the contoured frequency by altitude diagram (CFAD; Yuter and Houze 1995), the CFDD provides histograms of a variable as a function of the horizontal distance from a reference point toward some arbitrary direction. In this case, reflectivity histograms are computed as a function of the distance from FRS offshore toward 210° azimuth (i.e., roughly perpendicular to the LLJ–TTA interface) using hourly averages of PPI reflectivity (Fig. 11). As a result, changes in reflectivity relative to the LLJ–TTA interface can be detected.

Between 1300 and 1400 UTC 16 February (Fig. 12a) an increase in the mode of the reflectivity distribution is evident from ~50 km offshore (~20 dBZ_e) toward the coast (~28 dBZ_e), with a local maximum (~30 dBZ_e) at ~15 km offshore. The reflectivity distribution over the period 1400–1500 UTC (Fig. 12b) is characterized by more variability from ~20 km offshore compared with the previous hour, while the local maximum (~32 dBZ_e) migrates to within ~11 km of the coast. Between 1500 and 1600 UTC (Fig. 12c), the reflectivity distribution exhibits little variation from ~20 km offshore to farther offshore (~27–29 dBZ_e). The local reflectivity maximum keeps approaching the coast (~8 km) and has a larger magnitude (~33–35 dBZ_e). Increased variability of the reflectivity distribution is evident within 30 km of the coast during the period between 1600 and 1700 UTC (Fig. 12d).

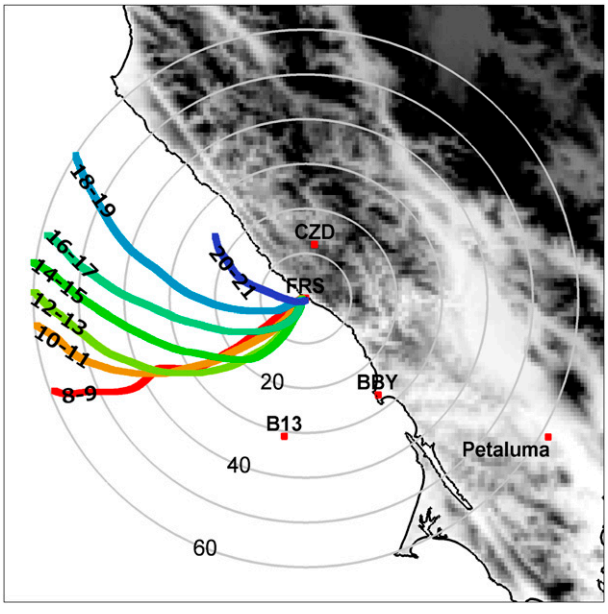

FIG. 9. Isochrones (in UTC on 16 Feb 2004) of the zero isodop observed in the average-PPI scans during episode 1. Colors represent the progression of time, from early (red) to late (blue) during the episode.

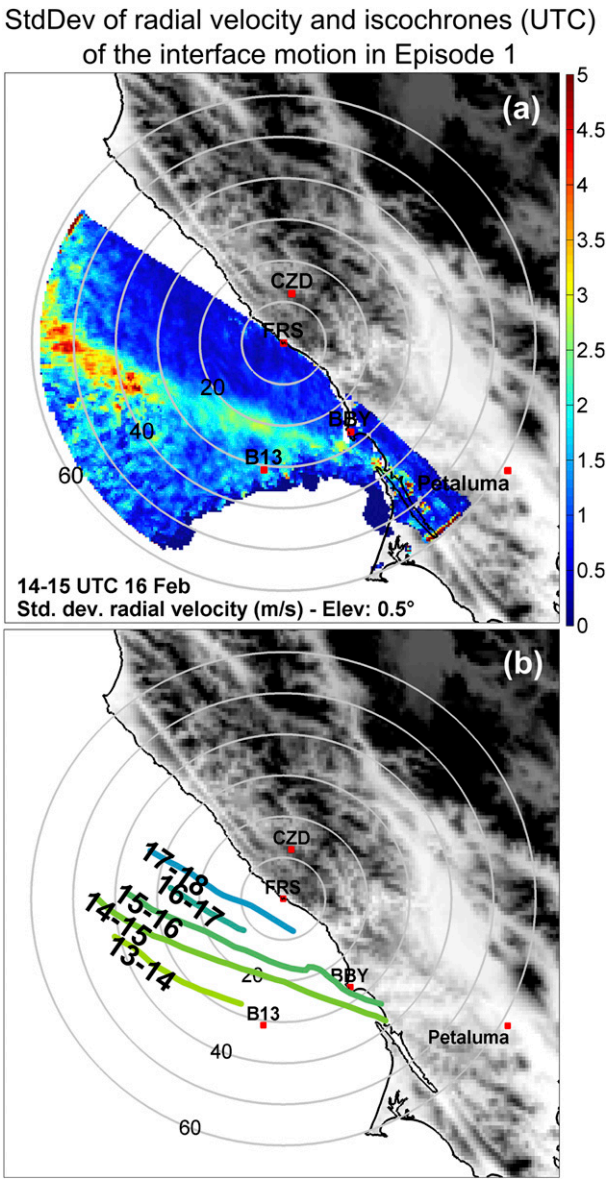

FIG. 10. (a) Standard deviation of the average PPI radial velocity ($m\,s^{-1}$) between 1400 and 1500 UTC 16 Feb showing a band (StdDev band) of large variation that highlights the LLJ–TTA interface motion during the analyzed hour. (b) Isochrones (in UTC on 16 Feb 2004) of the StdDev band observed during other hours in episode 1. Each isochrone is drawn along the edge of the StdDev band that is closest to the coast for each hour when the band was visually detected.

However, the dominant mode of the reflectivity distribution has a distinct maximum of ~36 dBZ_e at ~5 km offshore. By 1700–1800 UTC (Fig. 12e), the reflectivity distribution is approximately independent of the distance offshore (~27–29 dBZ_e) except within 5 km of the coast where modal values increase to ~34 dBZ_e.

The systematic progression of maximum reflectivity toward the coast documented in Fig. 12 represents local

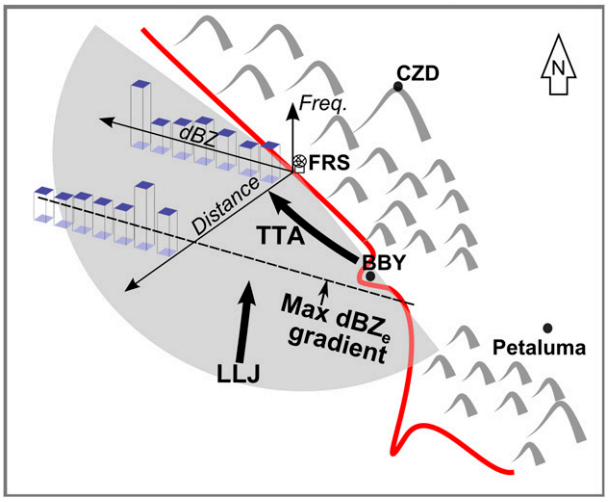

FIG. 11. Schematic illustration of the CFDD employed in this study. The gray-shaded area indicates the spatial domain of X-Pol PPI scans and the red line indicates the coastline. The orientation of the distance axis (reference azimuth) is chosen such that it is orthogonal to the maximum horizontal reflectivity gradient and the LLJ–TTA interface at 1400–1500 UTC 16 Feb (Fig. 7). Columns schematically represent the histograms that are built as a function of distance showing a hypothetical distribution: high frequency of large dBZ_e values near the coast and high frequency of low dBZ_e values offshore. LLJ indicates location and orientation of the low-level jet while TTA indicates location and orientation of terrain-trapped airflow.

precipitation enhancement due to the ascent of the incoming LLJ over the TTA. Cloud particles likely reach larger sizes just downwind of the LLJ–TTA interface because of the vertical ascent of the LLJ over the TTA and subsequent condensation. Then, once the LLJ stops its ascent and coalesced particles have fallen out, precipitation decays near the coast. Finally, close to the coastal mountains, direct orographic ascent likely contributes to the reflectivity maxima.

Thermodynamic characteristics associated with the TTA during episode 1 are documented with a time–height section of virtual potential temperature (θ_v) derived from the RASS at BBY (Fig. 13a). Results show that episode 1 is characterized by relatively cold temperatures between 0800 and 1600 UTC 16 February, with θ_v ~283–285 K at the surface and ~283–287 K in the lowest 500 m MSL above the surface in connection with east-southeasterly to southeasterly winds likely originating over the land. After 1600 UTC 16 February, temperatures increase to ~285–287 K at the surface and ~287–291 K in the lowest 500 m MSL above the surface in association with south-southeasterly to south-southwesterly winds, which likely originated over the ocean. Similarly, TTA characteristics at FRS in the lowest 500 m above the surface are examined using balloon-sounding observations at 1758 UTC

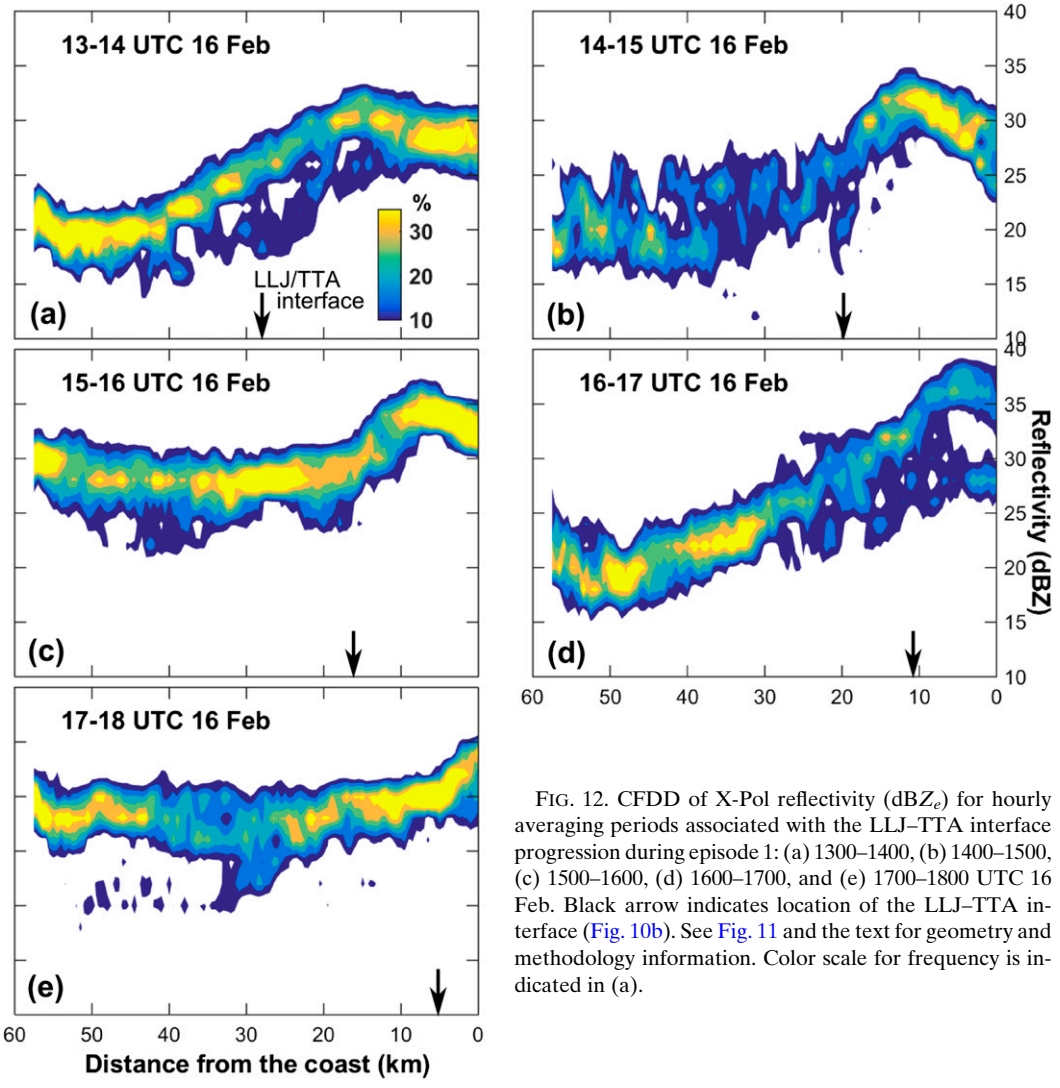

FIG. 12. CFDD of X-Pol reflectivity (dBZ_e) for hourly averaging periods associated with the LLJ–TTA interface progression during episode 1: (a) 1300–1400, (b) 1400–1500, (c) 1500–1600, (d) 1600–1700, and (e) 1700–1800 UTC 16 Feb. Black arrow indicates location of the LLJ–TTA interface (Fig. 10b). See Fig. 11 and the text for geometry and methodology information. Color scale for frequency is indicated in (a).

16 February (Fig. 13b). Equivalent potential temperature (θ_e) is nearly constant (307 K), indicative of moist-neutral conditions. Relative humidity (not shown) exhibits saturated conditions (i.e., >90%) from just above the surface to midlevels of the troposphere. Static stability is characterized with moist Brunt–Väisälä frequency (N_m; Durran and Klemp 1982), which indicates a mean value of $4.3 \times 10^{-3}\,s^{-1}$. Winds are southeasterly, with a slightly negative mean cross-barrier component of $-1.0\,m\,s^{-1}$. While further thermodynamic analysis is addressed in section 5, the air within the TTA in episode 1 is characterized by a ~500-m depth, relatively weak stratification, and a slightly downslope flow.

b. *Episode 2: 0600 UTC 17 February–0600 UTC 18 February 2004*

Sporadic LLJ structures are observed at BBY during episode 2 (Fig. 14a), with maximum meridional wind speeds of $\sim 30\,m\,s^{-1}$ centered at altitudes ranging from 0.6 to 1.2 km MSL. The wind direction in all these structures is between southerly to south-southwesterly and the distinctive vertical gradient of meridional wind speed observed during episode 1 at ~0.6–0.7 km is not apparent. After 2300 UTC 17 February there is a marked shift to much weaker winds. Above the surface, winds are mainly southwesterly and meridional speeds decrease from ~30 to $\sim 5\,m\,s^{-1}$. At the surface, winds are mainly south-southeasterly with meridional speeds of $\sim 10\,m\,s^{-1}$ that decrease to $\sim 5\,m\,s^{-1}$. This marked shift is most likely associated with a cold frontal passage described in section 3 (e.g., Fig. 2e). There were no high-elevation-angle X-Pol PPI scans executed during episode 2 to derive VAD wind profiles at FRS. As an alternative, balloon-sounding observations were employed to produce a time–height analysis of horizontal winds (Fig. 14b). This analysis suggests a comparable

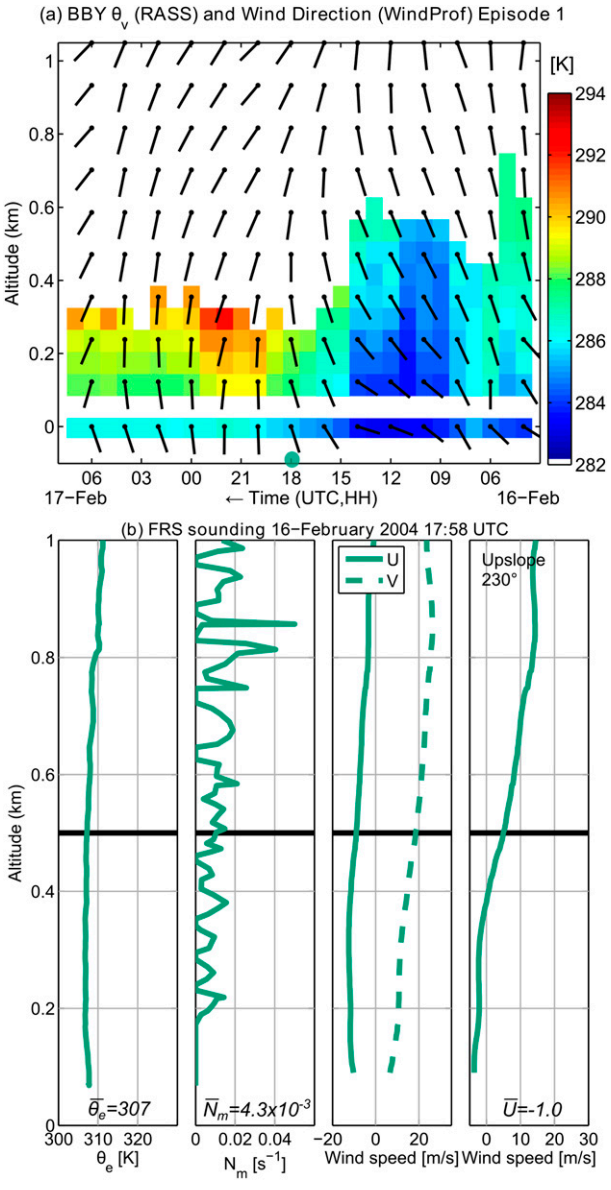

FIG. 13. (a) Time–height analysis of virtual potential temperature (θ_v) at BBY from RASS overlaid with total wind direction (wind staffs) from the 915-MHz wind profiler at the same location. The light green circle indicates time of balloon sounding release at FRS. Time is from right to left to represent eastward advection of the storm. (b) Balloon sounding profiles at FRS: equivalent potential temperature (θ_e), moist Brunt–Väisälä frequency (N_m), zonal (U) and meridional (V) wind components, and cross-barrier wind from 230°. Black horizontal lines indicate the 500-m altitude and mean-layer values are included.

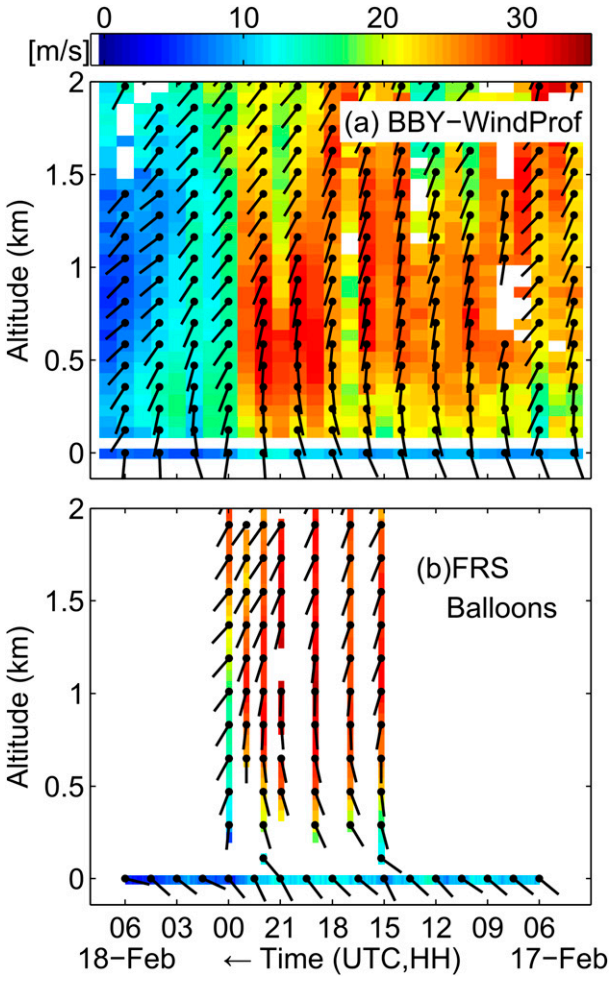

FIG. 14. Time–height analysis of meridional wind speed (color coded, m s^{-1}) and total wind direction (wind staffs) at (a) BBY from the 915-MHz wind profiler (WindProf) and (b) FRS from balloon soundings during episode 2 with same conventions as in Fig. 6. Balloon sounding profiles are centered at launch time and each have a 20-min window to improve visibility.

behavior at FRS relative to BBY above 0.5 km MSL, with meridional winds of ~30 m s^{-1} that significantly weaken after 2300 UTC 17 February. However, larger differences are evident below 0.5 km MSL, where FRS has weaker meridional wind speeds and slightly larger easterly component wind directions compared to BBY. The character of this low-level flow structure is further explored with PPI and RHI scans.

Average Doppler radial velocity during 1900–2000 UTC 17 February (Fig. 15a) shows a zero-isodop line indicative of a smooth south-southeasterly to south-southwesterly wind-direction transition. Zero-isodop lines from PPI averages at other hours over the course of episode 2 (not shown) but before the cold frontal passage (section 3, Fig. 2e) reveal little variation relative to the 19–20 UTC 17 February average. This wind-direction transition occurs out to a range of almost 60 km, which corresponds to a beam height of ~700 m MSL for a 0.5° PPI. The vertical gradient of wind direction at BBY (Fig. 14a) indicates a smooth south-southeasterly to south-southwesterly transition below

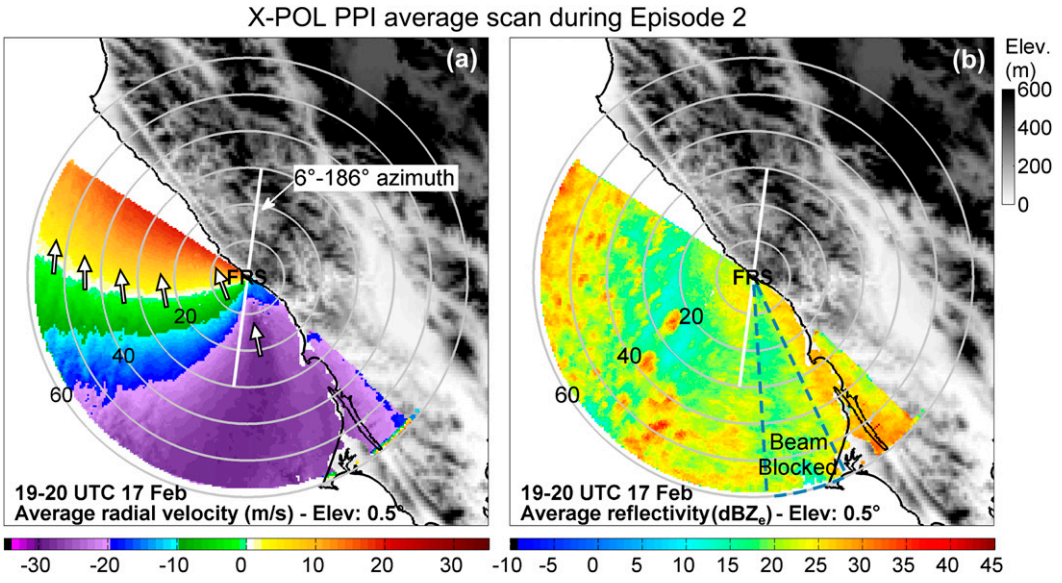

FIG. 15. As in Fig. 7, but during episode 2 between 1900 and 2000 UTC 17 Feb.

700 m MSL from 0800 to 2000 UTC 17 February, in agreement with inferences from the PPI averages. Therefore, unlike the sharply curved zero isodop observed in episode 1 associated with a strong horizontal gradient in wind direction due to the TTA, the smooth and broadly curved zero isodop observed in episode 2 is more likely produced by the background vertical gradient rather than the horizontal gradient in wind direction. As a consequence, the kinematic structure inferred from the X-Pol radial velocity suggests the absence of a TTA during episode 2.

The companion average reflectivity during 1900–2000 UTC 17 February (Fig. 15b) indicates background values of ~18 dBZ_e with embedded cells of ~35 dBZ_e. This pattern suggests scattered convective precipitation at this hour, which is representative of the pattern observed over extended periods of episode 2. However, the reflectivity enhancement observed offshore during episode 1 (e.g., Fig. 7) is absent at this hour and during the course of episode 2.

The vertical structure of horizontal winds and reflectivity is analyzed using hourly averages of RHI scans directed toward 6° azimuth (i.e., nearly north). These scans were executed with a maximum elevation angle of ~162° (i.e., ~18° elevation above the horizon), which allowed a view toward 186° azimuth (i.e., nearly south). The horizontal velocity between 1900 and 2000 UTC 17 February (Fig. 16a) shows the meridional component of the LLJ with a magnitude of ~30 m s^{-1} located over a weaker airflow of ~10 m s^{-1}. This kinematic structure varies only slightly during the course of episode 2. Although there is limited RHI context for offshore low-level airflow, we hypothesize that an upward-sloping LLJ is present immediately in advance of the coastal terrain as a result of direct orographic forcing (dashed line Fig. 16a), which is in stark contrast to the structure observed during episode 1. Given the absence of a TTA kinematic structure during episode 2, the weaker airflow residing below the LLJ and above the windward slope (also observed with FRS balloon soundings; Fig. 14b) is possibly due

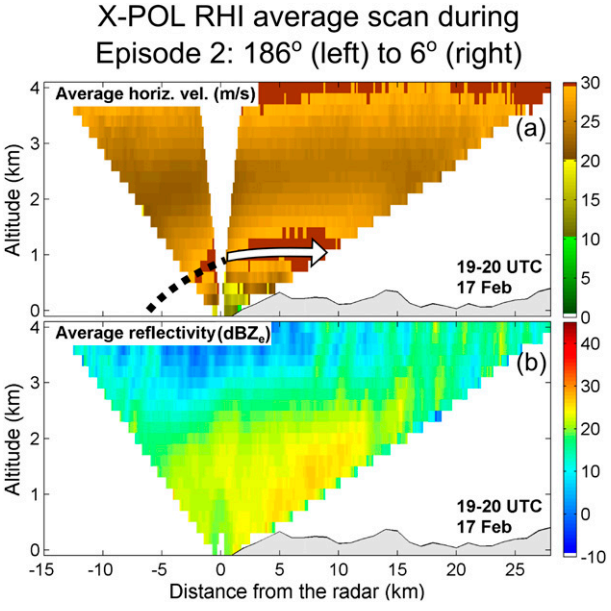

FIG. 16. As in Fig. 8, but during episode 2 between 1900 and 2000 UTC 17 Feb and with azimuth orientation of 186°–6°. Dashed line indicates hypothesized LLJ location offshore.

to the frictional effects of the terrain on the lower portion of the LLJ.

The companion average RHI-scan reflectivity between 1900 and 2000 UTC 17 February (Fig. 16b) exhibits echoes of ~18 dBZ_e below 2.5 km MSL, with maximum values of ~25–28 dBZ_e located above the windward slope and onshore over the coastal mountains. These results suggest that the absence of a TTA in episode 2 leads to the cross-barrier flow sloping upward directly over the orographic barrier, so precipitation over the coastal mountains tends to be larger relative to the coast as documented by the precipitation ratios in Table 2 and the hourly rain rates in Fig. 5.

Further contrast between the two episodes is documented with the thermodynamic characteristics of episode 2. Virtual potential temperatures at BBY (Fig. 17a) vary between ~288 and 290 K above the surface and ~286 K at the surface. Cooling of about 1–2 K after 0000 UTC 18 February is most likely associated with a cold-frontal passage (e.g., Figs. 2d,e). Hence, episode 2 is characterized by less variable and generally higher-valued BBY temperatures below 500 m compared to episode 1. A series of six balloon soundings released at FRS during the period from 1510 to 2259 UTC 17 February (Fig. 17b) indicates generally saturated conditions (i.e., RH > 90%; not shown) with $\overline{\theta_e}$ = 309 K, $\overline{N_m}$ = 4.6 × 10^{-3} s^{-1}, the mean wind direction out of the south-southeast, and a mean cross-barrier wind of 7.8 m s^{-1} in the layer below 500 m MSL. Interestingly, the mean static stability in the lowest 500 m above FRS observed during episode 2 in the absence of a TTA is almost the same as that observed during episode 1 with a noticeable TTA. This result is addressed in the following section.

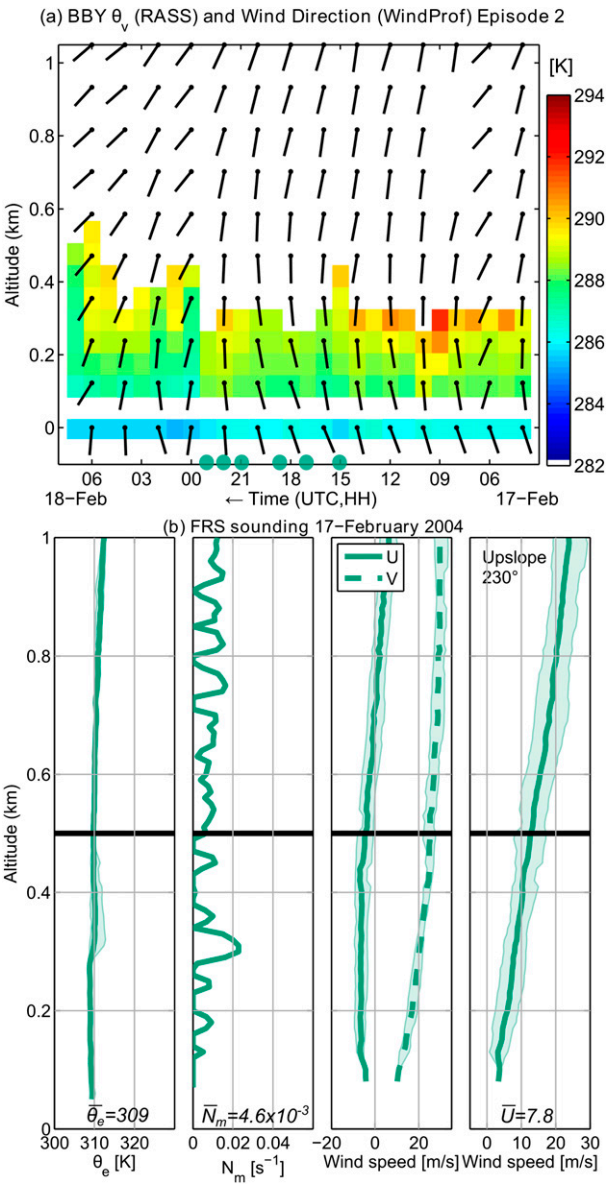

FIG. 17. As in Fig. 13, but for episode 2. Light green circles in (a) indicate launch time of single soundings. Light green lines in (b) indicate mean values considering six balloon soundings released at 1510, 1658, 1859, 2058, 2159, and 2259 UTC 17 Feb; shaded areas represent minimum and maximum ranges considering all these soundings.

5. Forcing of terrain-trapped airflow

As mentioned earlier, the TTA described in this study is associated with a relatively narrow air mass flowing poleward in close proximity and approximately parallel to the west side of the coastal orography. The TTA observed during episode 1 was well documented from a kinematic and thermodynamic perspective, but its dynamic forcing was not addressed. In this section, three hypotheses for forcing of the episode 1 TTA are examined: cold pool, low-level blocking, and gap flow.

A cold pool is typically formed in association with the downdrafts from precipitating convective cells (e.g., Engerer et al. 2008). In this process, raindrops evaporate within a subsaturated environment beneath cloud base, cooling the downdraft air and spreading out horizontally at the surface, forming a cold pool and potentially a density current structure (e.g., Markowski and Richardson 2010). Although some transient and small cellular-convection structures were observed during episode 1 (Figs. 7b–d), they crossed the observation domain in less than an hour, which makes it unlikely that they could produce a consolidated cold pool along the coast capable of forming the observed kinematic structure associated with the TTA. Even in the absence of convective cells, a cold pool formed by simple evaporative cooling seems unlikely since surface relative

humidity values at BBY, FRS, and CZD, as well as sounding profiles at FRS (not shown), are all between 85% and 100% from 0700 UTC 16 February onward, making it doubtful that subsaturated conditions could lead to cold pool formation. Therefore, a precipitation-generated cold pool along the coast is rejected as a hypothesis for explaining the TTA kinematic structure.

Low-level blocking on the windward side of mountain barriers is typically associated with stably stratified cross-barrier flows characterized by Fr [Eq. (1)] between 0 and 1 (Smith 1979). Calculation of Fr for episode 1 employs an interpretation of Eq. (1) similar to that used by Hughes et al. (2009) and Kingsmill et al. (2013). A barrier height (h) of 500 m MSL is assumed, which represents an average altitude of nearby coastal mountain peaks within a radius of 40 km from FRS. Here, N is calculated within the perturbed air associated with the TTA and obtained from the lowest 500 m of the 1758 UTC 16 February balloon sounding at FRS (Fig. 13b). Given the saturated conditions (i.e., RH $>$ 90%) observed in this layer (not shown), N_m is the most appropriate theoretical reference with a value of $4.3 \times 10^{-3}\,s^{-1}$. Average cross-barrier wind speed (U, from 230°) in the lowest 500 m is derived upstream of the perturbed airflow associated with the TTA using X-Pol RHI and PPI observations at ~1758 UTC 16 February. Winds in this layer are estimated at a range of ~30 km along the 180° radial from FRS. This location provides an estimate of wind conditions upwind (i.e., to the south) of the LLJ–TTA interface (see Fig. 10b), which is presumably also the offshore extent of stable air associated with the TTA. The 180° RHI scan (not shown) allows derivation of the TTA-layer mean meridional flow upstream of the TTA. A nearly coincident X-Pol PPI scan at 0.5°-elevation angle (not shown) provides an estimate of low-level wind direction to facilitate the calculation of U from the RHI scan. This approach yields U equal to $20\,m\,s^{-1}$. Combining the estimates of h, N_m, and U produces Fr equal to 9.3, indicating that the TTA is unlikely forced by low-level blocking. The absence of low-level blocking may explain why similar stabilities were observed in the TTA layer during episodes 1 and 2 despite the dramatic differences in kinematic structure.

Gap flows are produced in mountainous regions where a relatively cold air mass crosses through gaps in the terrain as a response to pressure gradients associated with approaching synoptic-scale disturbances. Neiman et al. (2006) examined several gap-flow cases along the coast of Northern California and found that a relatively cold airflow of ~500-m depth frequently exited the Central Valley through the Petaluma Gap (Fig. 1b) and crossed over BBY. With this as context, the joint behavior between along-gap pressure difference and the zonal wind at BBY during episode 1 of the present case study is now examined. The hourly pressure difference between BBY and a METAR station located over California's Central Valley at Stockton (SCK) provides a direct measure of the along-gap pressure gradient (Fig. 1b). Zonal winds were derived using surface and 0–500-m layer-mean (TTA layer) observations at BBY from the 915-MHz wind profiler. These data were temporally segregated before and after 1600 UTC 16 February when temperatures below 500 m MSL at BBY transitioned from relatively cold to relatively warm (Fig. 13a). This time is also coincident with the LLJ–TTA interface passage over BBY (Fig. 10). The theoretical relationship between gap flow, pressure gradient, and friction is also explored by using the M95 equation [Eq. (2)]. The original drag coefficient ($C_D = 7.5 \times 10^{-3}$) was varied by ±50% to evaluate the parameter space associated with frictional forces. Wind speed at the gap entrance [$u(0)$] was assumed to be zero since its effect is negligible at the gap exit (100 km downwind). An average air density of $1.24\,kg\,m^{-3}$ derived from observations at BBY and SCK was employed.

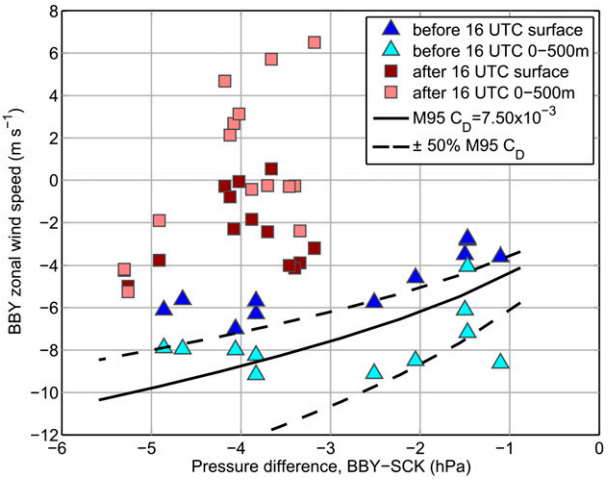

FIG. 18. Scatterplot of hourly surface pressure difference between BBY and SCK vs hourly zonal winds at BBY at surface level (dark blue, dark red) and averaged in the 0–500-m layer (light blue, light red). Observations were segregated between observations before (tringles, inclusive) and after (squares) 1600 UTC 16 Feb based on θ_v observations (Fig. 13). Black lines represent the theoretical relationship between pressure gradient, surface friction, and gap flow winds provided by M95 (solid black line) with a ±50% variation in the drag coefficient (C_D, dashed black line).

Figure 18 reveals that temporal separation of the observations produces two different patterns of behavior. The group before 1600 UTC (relatively cold near-surface temperatures) tends to follow the force balance given by the M95 equation. Surface outliers could

be due to underestimation of the drag coefficient (i.e., the actual C_D is larger than $1.5C_D$ in M95). Also, since BBY is located west of the Petaluma Gap and therefore exposed to airflows other than the Petaluma Gap flow, the 0–500-m outliers could be associated with transient mesoscale features ahead of the approaching warm front (see section 3). In contrast, the group after 1600 UTC (relatively warmer temperatures) significantly departs from the M95 equation, suggesting that these observations are not associated with a gap flow. Given that low-level winds over BBY up to 1600 UTC 16 February are identified as part of the TTA, this analysis favors the hypothesis that a gap flow forces the TTA. As a result, airflow exiting the Petaluma Gap should have a right-turning curvature. This horizontal airflow pattern may explain the skewed orientation of the LLJ–TTA interface documented in Fig. 10, where positions are farther offshore toward the north.

6. Summary and conclusions

This study has documented orographic precipitation forcing along the coastal mountains of Northern California during the landfall of a significant winter storm over the period 16–18 February 2004. Observations from scanning and profiling Doppler radars, balloon soundings, a radio acoustic sounding system (RASS), buoys, a GPS receiver, and surface meteorological sensors were part of the instrumentation employed. The scanning Doppler radar (X-Pol) located near sea level on the coast was the main asset used to document the kinematic and precipitation structure offshore and along the coast since it provided horizontal and vertical context near the surface.

The landfalling winter storm was associated with a synoptic-scale cyclonic circulation over the Pacific moving eastward. Warm and cold frontal passages, low-level jet (LLJ) structures, and the landfall of an atmospheric river (AR) were also evident. The event was divided into two 24-h-duration episodes (episode 1 starting at 0600 UTC 16 February and episode 2 starting at 0600 UTC 17 February) based on different surface rain-rate characteristics along the coast.

LLJ structures were characteristics of both episodes; however, a terrain-trapped airflow (TTA) structure was observed only during episode 1. A schematic that summarizes the kinematic and precipitation structure associated with the LLJ and TTA interaction is presented in Fig. 19. The TTA structure was observed for ~5 h and up to ~25 km offshore of the coastline with a depth of ~0.5 km MSL. As episode 1 progressed, the LLJ–TTA interface moved closer to shore with a skewed orientation relative to the mean coastline orientation such that positions are farther offshore toward the north. Meanwhile, the incoming LLJ sloped from an average altitude of ~0.25 km MSL offshore to ~1 km MSL over the coast. FRS presented a weakly stratified atmosphere associated with the TTA; hence, the LLJ was probably displaced upward through isentropic lift because horizontally moving air parcels would tend to conserve their potential temperature (e.g., Saucier 1989; Neiman et al. 2002).

A precipitation enhancement zone was observed offshore in association with convergence from the LLJ–TTA interface. The precipitation enhancement zone moved toward the coast as the LLJ–TTA interface moved coastward. Convergence produced by synoptic flows (e.g., LLJ) and TTAs has been previously documented, such as in Neiman et al. (2004), Yu et al. (2007), and Yu and Hsieh (2009). However, while the former studies document the origin of the TTA as low-level blocking, the present study documents a TTA formed by an offshore-directed gap flow.

During episode 2, the kinematic structure along the coast and offshore was fundamentally different. The LLJ–TTA interface was absent, so that the LLJ sloped upward directly over the windward side of the coastal mountains. Consequently, orographic precipitation enhancement over the coastal mountain was likely achieved through an upslope flow effect (i.e., forced ascent by the orography).

The contrast between episodes 1 and 2 in terms of LLJ lifting (offshore and onshore, respectively) and the precipitation enhancement response is consistent with the observed mountain (CZD) to coastal (FRS and BBY) precipitation ratios (average of 1.2 in episode 1 and 4.2 in episode 2; Table 2), as well as with previous studies [0.71 blocked and 5.6 unblocked; Neiman et al. (2002)]. Hourly rain rates (Fig. 5a) are also in agreement with offshore and onshore lifting, showing consistently larger rain rates over FRS and BBY for several hours during episode 1 and larger rain rates over CZD during almost the entire course of episode 2.

Forcing of the TTA was investigated by analyzing cold pool, low-level blocking and gap-flow hypotheses. This analysis favored the hypothesis that the TTA is forced by a gap flow exiting the Petaluma Gap that encounters the onshore airstream associated with the LLJ–TTA formation in this manner is consistent with previous studies performed along the Gulf of Alaska (Loescher et al. 2006). Since offshore-directed gap flows in the Northern Hemisphere have a right-turning curvature, this forcing mechanism could explain the observed skewed orientation of the LLJ–TTA interface where positions are farther offshore toward the north.

Although thermodynamic characteristics associated with the TTA along the coast were documented, profiling RASS and balloon soundings only provided observations

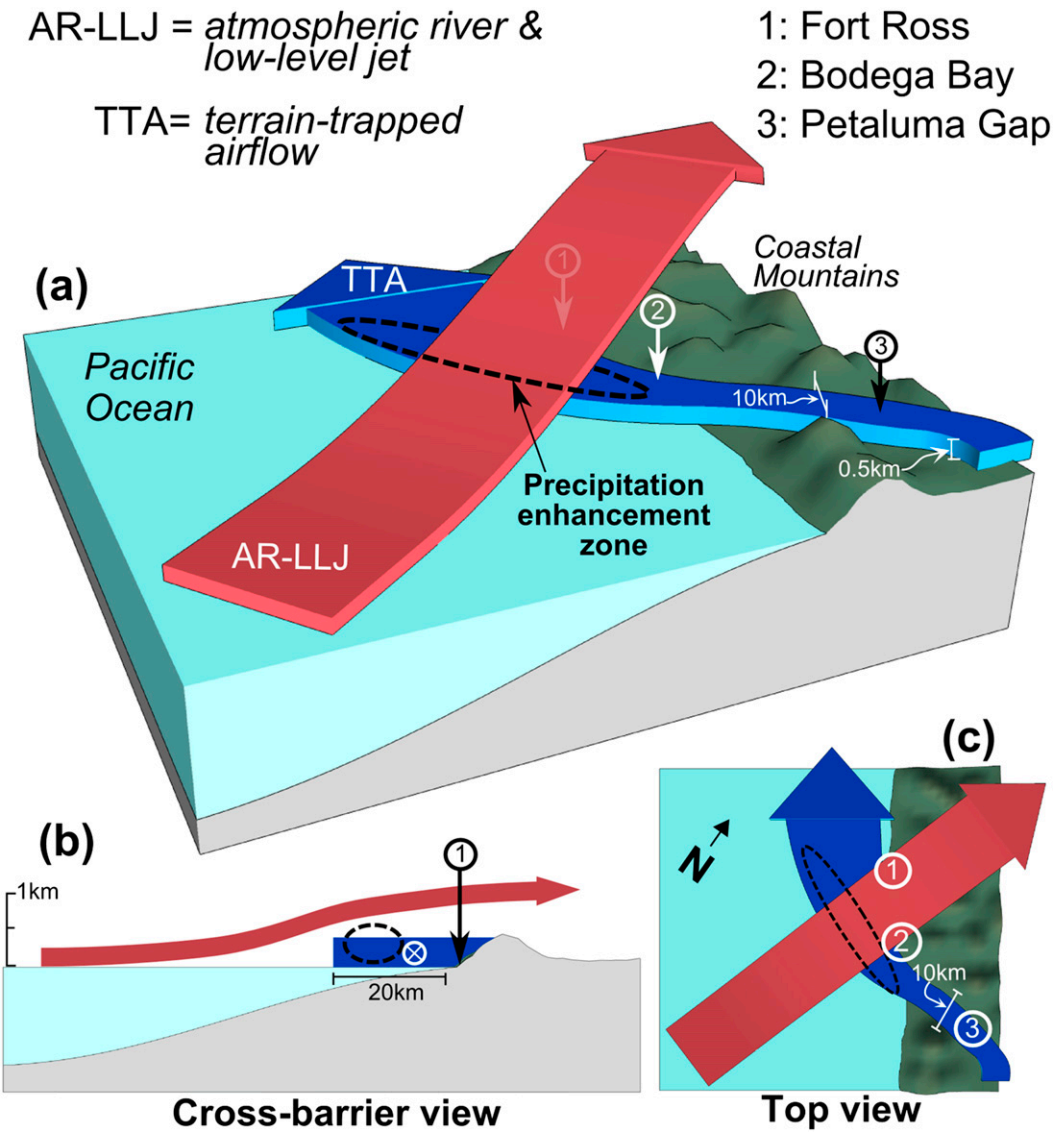

FIG. 19. (a) Three-dimensional schematic illustration depicting the kinematic structure of the AR–LLJ (red arrow) and TTA (blue arrow) observed during this study. (b) Cross-barrier and (c) top view of the schematic in (a). Dashed black line indicates the zone of enhanced precipitation due to the LLJ–TTA interface forcing. White crossed circled in (b) indicates airflow toward the page. The offshore extension of the TTA represents observations during 1400–1500 UTC 16 Feb (e.g., Figs. 7 and 8a,c).

at single points (BBY and FRS, respectively) and were sparse in time in the case of the balloon soundings. As a result, it is unclear if mixing was occurring at the LLJ–TTA interface and if that could have affected the lifting of the LLJ. In addition, it is interesting to contrast these results with Neiman et al. (2006), whose gap-flow inventory does not account for the case presented here (perhaps corresponding to a weaker-than-normal gap-flow case) and who found that a linear relationship between pressure difference and zonal wind best represented a 5-day gap-flow case. Since in our case study a linear relationship is less clear, one remaining question is the relative importance of frictional forces in determining gap-flow magnitude. Another remaining question relates to the representativeness of the kinematic and precipitation structures observed in this case relative to other winter storm cases within the same domain. This question will be addressed in future research by the authors.

Acknowledgments. The authors thank the NOAA/ESRL observing systems team for deploying and operating the instrumentation whose data were employed in this

study. Gary Wick of ESRL generated the SSM/I IWV images. Timothy Coleman of ESRL processed the wind profiler and RASS data. We appreciate the comments and suggestions of Paul Neiman, Mimi Hughes, Matthias Steiner, and Katja Friedrich that have been provided during the course of this study. Similarly, comments and suggestions from three anonymous reviewers helped to improve the manuscript. RV is supported by the Fulbright Program and CONICYT-Chile. This research was sponsored by NSF under Grant AGS-1144271.

REFERENCES

Anders, A. M., G. H. Roe, D. R. Durran, and J. R. Minder, 2007: Small-scale spatial gradients in climatological precipitation on the Olympic Peninsula. *J. Hydrometeor.,* **8,** 1068–1081, doi:10.1175/JHM610.1.

Bergeron, T., 1965: On the low-level redistribution of atmospheric water caused by orography. *Proc. Int. Conf. Cloud Physics* (Suppl.), Tokyo, Japan, International Association of Meteorology and Atmospheric Physics, 96–100.

Bousquet, O., and B. F. Smull, 2003: Observations and impacts of upstream blocking during a widespread orographic precipitation event. *Quart. J. Roy. Meteor. Soc.,* **129,** 391–409, doi:10.1256/qj.02.49.

Browning, K. A., and R. Wexler, 1968: The determination of kinematic properties of a wind field using Doppler radar. *J. Appl. Meteor.,* **7,** 105–113, doi:10.1175/1520-0450(1968)007<0105:TDOKPO>2.0.CO;2.

——, F. F. Hill, and C. W. Pardoe, 1974: Structure and mechanism of precipitation and the effect of orography in a wintertime warm sector. *Quart. J. Roy. Meteor. Soc.,* **100,** 309–330, doi:10.1002/qj.49710042505.

Businger, S., and Coauthors, 1996: The promise of GPS in atmospheric monitoring. *Bull. Amer. Meteor. Soc.,* **77,** 5–18, doi:10.1175/1520-0477(1996)077<0005:TPOGIA>2.0.CO;2.

Carter, D. A., K. S. Gage, W. L. Ecklund, W. M. Angevine, P. E. Johnston, A. C. Riddle, J. Wilson, and C. R. Williams, 1995: Developments in UHF lower tropospheric wind profiling at NOAA's Aeronomy Laboratory. *Radio Sci.,* **30,** 977–1001, doi:10.1029/95RS00649.

Clifford, S. F., J. C. Kaimal, R. J. Lataitis, and R. G. Strauch, 1994: Ground-based remote profiling in atmospheric studies: An overview. *Proc. IEEE,* **82,** 313–355, doi:10.1109/5.272138.

Colle, B. A., and C. F. Mass, 2000: High-resolution observations and numerical simulations of easterly gap flow through the Strait of Juan de Fuca on 9–10 December 1995. *Mon. Wea. Rev.,* **128,** 2398–2422, doi:10.1175/1520-0493(2000)128<2398:HROANS>2.0.CO;2.

Durran, D. R., and J. B. Klemp, 1982: On the effects of moisture on the Brunt–Väisälä frequency. *J. Atmos. Sci.,* **39,** 2152–2158, doi:10.1175/1520-0469(1982)039<2152:OTEOMO>2.0.CO;2.

Eckhardt, S., A. Stohl, H. Wernli, P. James, C. Forster, and N. Spichtinger, 2004: A 15-year climatology of warm conveyor belts. *J. Climate,* **17,** 218–237, doi:10.1175/1520-0442(2004)017<0218:AYCOWC>2.0.CO;2.

Ecklund, W. L., D. A. Carter, and B. B. Balsley, 1988: A UHF wind profiler for the boundary layer: Brief description and initial results. *J. Atmos. Oceanic Technol.,* **5,** 432–441, doi:10.1175/1520-0426(1988)005<0432:AUWPFT>2.0.CO;2.

Engerer, N. A., D. J. Stensrud, and M. C. Coniglio, 2008: Surface characteristics of observed cold pools. *Mon. Wea. Rev.,* **136,** 4839–4849, doi:10.1175/2008MWR2528.1.

Fischler, M. A., and R. C. Bolles, 1981: Random sample consensus: a paradigm for model fitting with applications to image analysis and automated cartography. *Commun. ACM,* **24,** 381–395, doi:10.1145/358669.358692.

Harrold, T. W., 1973: Mechanisms influencing the distribution of precipitation within baroclinic disturbances. *Quart. J. Roy. Meteor. Soc.,* **99,** 232–251, doi:10.1002/qj.49709942003.

Hughes, M., A. Hall, and R. G. Fovell, 2009: Blocking in areas of complex topography, and its influence on rainfall distribution. *J. Atmos. Sci.,* **66,** 508–518, doi:10.1175/2008JAS2689.1.

James, C. N., and R. A. Houze, 2005: Modification of precipitation by coastal orography in storms crossing northern California. *Mon. Wea. Rev.,* **133,** 3110–3131, doi:10.1175/MWR3019.1.

Kingsmill, D. E., P. J. Neiman, B. J. Moore, M. Hughes, S. E. Yuter, and F. M. Ralph, 2013: Kinematic and thermodynamic structures of Sierra barrier jets and overrunning atmospheric rivers during a landfalling winter storm in northern California. *Mon. Wea. Rev.,* **141,** 2015–2036, doi:10.1175/MWR-D-12-00277.1.

Lackmann, G. M., and J. E. Overland, 1989: Atmospheric structure and momentum balance during a gap-wind event in Shelikof Strait, Alaska. *Mon. Wea. Rev.,* **117,** 1817–1833, doi:10.1175/1520-0493(1989)117<1817:ASAMBD>2.0.CO;2.

Loescher, K., G. Young, B. A. Colle, and N. S. Winstead, 2006: Climatology of barrier jets along the Alaskan coast. Part I: Spatial and temporal distributions. *Mon. Wea. Rev.,* **134,** 437–453, doi:10.1175/MWR3037.1.

Markowski, P., and Y. Richardson, 2010: *Mesoscale Meteorology in Midlatitudes.* Wiley-Blackwell, 407 pp.

Martner, B. E., K. A. Clark, S. Y. Matrosov, W. C. Campbell, and J. S. Gibson, 2001: NOAA/ETL's polarization-upgraded x-band "hydro" radar. Preprints, *30th Int. Conf. on Radar Meteorology,* Munich, Germany, Amer. Meteor. Soc., P3.5. [Available online at https://ams.confex.com/ams/pdfpapers/21364.pdf.]

Marwitz, J. D., 1983: The kinematics of orographic airflow during Sierra storms. *J. Atmos. Sci.,* **40,** 1218–1227, doi:10.1175/1520-0469(1983)040<1218:TKOOAD>2.0.CO;2.

Mass, C. F., S. Businger, M. D. Albright, and Z. A. Tucker, 1995: A windstorm in the lee of a gap in a coastal mountain barrier. *Mon. Wea. Rev.,* **123,** 315–331, doi:10.1175/1520-0493(1995)123<0315:AWITLO>2.0.CO;2.

Matrosov, S. Y., D. E. Kingsmill, and B. E. Martner, 2005: The utility of x-band polarimetric radar for quantitative estimate of rainfall parameters. *J. Hydrometeor.,* **6,** 248–262, doi:10.1175/JHM424.1.

Mayr, G. J., and Coauthors, 2007: Gap flows: Results from the Mesoscale Alpine Programme. *Quart. J. Roy. Meteor. Soc.,* **133,** 881–896, doi:10.1002/qj.66.

Minder, J. R., and D. E. Kingsmill, 2013: Mesoscale variations of the atmospheric snow line over the northern Sierra Nevada: multiyear statistics, case study, and mechanisms. *J. Atmos. Sci.,* **70,** 916–938, doi:10.1175/JAS-D-12-0194.1.

Neiman, P. J., P. T. May, and M. A. Shapiro, 1992: RASS and wind profiler observations of lower- and midtropospheric weather systems. *Mon. Wea. Rev.,* **120,** 2298–2313, doi:10.1175/1520-0493(1992)120<2298:RASSAW>2.0.CO;2.

——, F. M. Ralph, A. B. White, D. E. Kingsmill, and P. O. G. Persson, 2002: The statistical relationship between upslope flow and rainfall in California's coastal mountains: Observations during CALJET. *Mon. Wea. Rev.,* **130,** 1468–1492, doi:10.1175/1520-0493(2002)130<1468:TSRBUF>2.0.CO;2.

——, P. O. G. Persson, F. M. Ralph, D. P. Jorgensen, A. B. White, and D. E. Kingsmill, 2004: Modification of fronts and precipitation by coastal blocking during an intense landfalling winter storm in southern California: Observations during CALJET. *Mon. Wea. Rev.,* **132,** 242–273, doi:10.1175/1520-0493(2004)132<0242:MOFAPB>2.0.CO;2.

——, F. M. Ralph, A. B. White, D. Parrish, J. S. Holloway, and D. L. Bartels, 2006: A multiwinter analysis of channeled flow through a prominent gap along the northern California coast during CALJET and PACJET. *Mon. Wea. Rev.,* **134,** 1815–1841, doi:10.1175/MWR3148.1.

——, ——, G. A. Wick, J. D. Lundquist, and M. D. Dettinger, 2008: Meteorological characteristics and overland precipitation impacts of atmospheric rivers affecting the west coast of North America based on eight years of SSM/I satellite observations. *J. Hydrometeor.,* **9,** 22–47, doi:10.1175/2007JHM855.1.

——, D. J. Gottas, A. B. White, S. I. Gutman, and F. M. Ralph, 2009: A water vapour flux tool for precipitation forecasting. *Proc. ICE-Water Manage.,* **162,** 83–94, doi:10.1680/wama.2009.162.2.83.

Overland, J. E., 1984: Scale analysis of marine winds in straits and along mountainous coasts. *Mon. Wea. Rev.,* **112,** 2530–2534, doi:10.1175/1520-0493(1984)112<2530:SAOMWI>2.0.CO;2.

——, and B. A. Walter, 1981: Gap winds in the Strait of Juan de Fuca. *Mon. Wea. Rev.,* **109,** 2221–2233, doi:10.1175/1520-0493(1981)109<2221:GWITSO>2.0.CO;2.

Pierrehumbert, R. T., and B. Wyman, 1985: Upstream effects of mesoscale mountains. *J. Atmos. Sci.,* **42,** 977–1003, doi:10.1175/1520-0469(1985)042<0977:UEOMM>2.0.CO;2.

Ralph, F. M., P. J. Neiman, and G. A. Wick, 2004: Satellite and CALJET aircraft observations of atmospheric rivers over the eastern North Pacific Ocean during the winter of 1997/98. *Mon. Wea. Rev.,* **132,** 1721–1745, doi:10.1175/1520-0493(2004)132<1721:SACAOO>2.0.CO;2.

——, ——, and R. Rotunno, 2005: Dropsonde observations in low-level jets over the northeastern Pacific Ocean from CALJET-1998 and PACJET-2001: Mean vertical-profile and atmospheric-river characteristics. *Mon. Wea. Rev.,* **133,** 889–910, doi:10.1175/MWR2896.1.

——, ——, G. A. Wick, S. I. Gutman, M. D. Dettinger, D. R. Cayan, and A. B. White, 2006: Flooding on California's Russian River: Role of atmospheric rivers. *Geophys. Res. Lett.,* **33,** L13801, doi:10.1029/2006GL026689.

——, and Coauthors, 2013: The emergence of weather-related test beds linking research and forecasting operations. *Bull. Amer. Meteor. Soc.,* **94,** 1187–1211, doi:10.1175/BAMS-D-12-00080.1.

Rutledge, S., and P. Hobbs, 1983: The mesoscale and microscale structure and organization of clouds and precipitation in midlatitudes cyclones. VIII: A model for the "seeder-feeder" process. *J. Atmos. Sci.,* **40,** 1185–1206, doi:10.1175/1520-0469(1983)040<1185:TMAMSA>2.0.CO;2.

Saha, S., and Coauthors, 2010: The NCEP Climate Forecast System Reanalysis. *Bull. Amer. Meteor. Soc.,* **91,** 1015–1057, doi:10.1175/2010BAMS3001.1.

Saucier, W. J., 1989: *Principles of Meteorological Analysis.* Dover Publications, 438 pp.

Schultz, D. M., 2001: Reeximaning the cold conveyor belt. *Mon. Wea. Rev.,* **129,** 2205–2225, doi:10.1175/1520-0493(2001)129<2205:RTCCB>2.0.CO;2.

Smith, R., 1979: The influence of mountains on the atmosphere. *Advances in Geophysics,* Vol. 21, Academic Press, 87–230.

Steenburgh, W. J., D. M. Schultz, and B. A. Colle, 1998: The structure and evolution of gap outflow over the Gulf of Tehuantepec, Mexico. *Mon. Wea. Rev.,* **126,** 2673–2691, doi:10.1175/1520-0493(1998)126<2673:TSAEOG>2.0.CO;2.

Trapp, R. J., and C. A. Doswell, 2000: Radar data objective analysis. *J. Atmos. Oceanic Technol.,* **17,** 105–120, doi:10.1175/1520-0426(2000)017<0105:RDOA>2.0.CO;2.

Weber, B. L., D. B. Wuertz, and D. C. Welsh, 1993: Quality controls for profiler measurements of winds and RASS temperatures. *J. Atmos. Oceanic Technol.,* **10,** 452–464, doi:10.1175/1520-0426(1993)010<0452:QCFPMO>2.0.CO;2.

Wentz, F. J., 1997: A well-calibrated ocean algorithm for Special Sensor Microwave/Imager. *J. Geophys. Res.,* **102,** 8703–8718, doi:10.1029/96JC01751.

Wick, G. A., P. J. Neiman, and F. M. Ralph, 2013: Description and validation of an automated objective technique for identification and characterization of the integrated water vapor signature of atmospheric rivers. *IEEE Trans. Geosci. Remote Sens.,* **51,** 2166–2176, doi:10.1109/TGRS.2012.2211024.

Wolfe, D., and S. I. Gutman, 2000: Developing an operational, surface-based, GPS, water vapor observing system for NOAA: Network design and results. *J. Atmos. Oceanic Technol.,* **17,** 426–440, doi:10.1175/1520-0426(2000)017<0426:DAOSBG>2.0.CO;2.

Wood, V. T., and R. A. Brown, 1986: Single Doppler velocity signature interpretation of nondivergent environmental winds. *J. Atmos. Oceanic Technol.,* **3,** 114–128, doi:10.1175/1520-0426(1986)003<0114:SDVSIO>2.0.CO;2.

Yu, C.-K., and B. F. Smull, 2000: Airborne Doppler observations of a landfalling cold front upstream of steep coastal orography. *Mon. Wea. Rev.,* **128,** 1577–1603, doi:10.1175/1520-0493(2000)128<1577:ADOOAL>2.0.CO;2.

——, and N. A. Bond, 2002: Airborne Doppler observations of a cold front in the vicinity of Vancouver Island. *Mon. Wea. Rev.,* **130,** 2692–2708, doi:10.1175/1520-0493(2002)130<2692:ADOOAC>2.0.CO;2.

——, and Y.-H. Hsieh, 2009: Formation of the convective lines off the mountainous coast of southeastern Taiwan: A case study of 3 January 2004. *Mon. Wea. Rev.,* **137,** 3072–3091, doi:10.1175/2009MWR2867.1.

——, D. P. Jorgensen, and F. Roux, 2007: Multiple precipitation mechanisms over mountains observed by airborne Doppler radar during MAP IOP5. *Mon. Wea. Rev.,* **135,** 955–984, doi:10.1175/MWR3318.1.

Yuter, S. E., and R. A. Houze, 1995: Three-dimensional kinematic and microphysical evolution of Florida cumulonimbus. Part II: Frequency distributions of vertical velocity, reflectivity, and differential reflectivity. *Mon. Wea. Rev.,* **123,** 1941–1963, doi:10.1175/1520-0493(1995)123<1941:TDKAME>2.0.CO;2.

Zhu, Y., and R. E. Newell, 1994: Atmospheric rivers and bombs. *Geophys. Res. Lett.,* **21,** 1999–2002, doi:10.1029/94GL01710.

——, and ——, 1998: A proposed algorithm for moisture fluxes from atmospheric rivers. *Mon. Wea. Rev.,* **126,** 725–735, doi:10.1175/1520-0493(1998)126<0725:APAFMF>2.0.CO;2.